

NASA Technical Paper 1187

Aerodynamic Heating in Gaps of Thermal Protection System Tile Arrays in Laminar and Turbulent Boundary Layers

Don E. Avery
*Langley Research Center
Hampton, Virginia*



National Aeronautics
and Space Administration

**Scientific and Technical
Information Office**

1978

SUMMARY

An experimental heat-transfer investigation was conducted using metallic tiles arranged in two staggered tile arrays with longitudinal and transverse gaps between the tiles. This tile arrangement results in longitudinal gaps terminating at intersections with transverse gaps. A direct impingement of the longitudinal gap flow on the forward face of a downstream blocking tile results; hence, high localized heating occurs at this impingement region. The tile arrays were tested (1) to define the impingement heating distributed on a downstream blocking tile and (2) to determine the influence of tile and gap geometries in sufficient detail to develop empirical relationships for impingement heating in laminar and turbulent boundary layers. The tests were conducted in the Langley 8-foot high-temperature structures tunnel at a nominal Mach number of 7, a nominal total temperature of 1800 K, and free-stream unit Reynolds numbers from 1.0×10^6 to 4.8×10^6 per m. Tile forward-facing wall slopes of 60° , 75° , and 90° were tested along with longitudinal gap lengths of 15.24 and 30.48 cm and gap widths of 0.10, 0.18, 0.30, and 0.41 cm. The boundary-layer displacement thickness covered a range from 0.36 to 1.62 cm. No laminar data were obtained on the 90° tile array. Flat-plate calibration tests provided comparison data.

For laminar boundary layers, the heating rates observed on the downstream blocking tile in the transverse gap direction for gap widths of 0.10 and 0.18 cm indicate that the gap flow is primarily two-dimensional in nature (i.e., flow in the longitudinal gap does not turn and flow in a transverse gap). Thus, the longitudinal gap flow has a negligible effect on the heating rates on the blocking tile for gap widths less than 0.18 cm. For a gap width of 0.41 cm, the heating rates in the transverse direction are less uniform. This lack of uniformity suggests that the basic flow is three-dimensional and that the flow in the longitudinal gap is becoming more influential. The data indicate that the maximum impingement heating of 2.4 times the flat-plate heating rate occurs for a gap width of 0.41 cm, and for the two smaller gap widths, the impingement heating was less than the surface heating. For turbulent boundary layers, the flow in the transverse gap is primarily three-dimensional in nature. The region affected by the three-dimensional flow extends at least three gap widths in the transverse and longitudinal directions. The maximum heating rate observed was 4.5 times the surface heating rate and occurred for a forward-facing wall slope of 90° and a gap width of 0.41 cm. Changing the slope of the forward-facing wall from 90° to 60° decreased the heating substantially in the impingement region. Decreasing the gap width also causes a decrease in impingement heating. In both laminar and turbulent flow the presence of gaps influences surface heating.

Empirical relationships to correlate impingement heating with gap flow and geometric parameters for laminar and turbulent flow were developed through combined regression analysis and graphic techniques. These relationships accurately predict the impingement heating rate and the influence of gap flow and geometric parameters within the data range used to develop the relationships.

INTRODUCTION

The thermal protection system (TPS) of the space shuttle orbiter consists of a silica-based material for the reusable surface insulation (RSI). The RSI is bonded to a strain isolator pad which is bonded to the primary structure and must withstand temperatures of approximately 1700 K on the bottom surface of the orbiter and maintain a primary structure temperature below 450 K during entry. Arranged in a staggered pattern, the RSI tiles are applied to the surface with gaps between tiles to accommodate thermal expansion and contraction and mechanical deflections of the underlying structure as well as to allow for thermal expansion of the tile material. The tiles are nominally 15 by 15 cm and the thickness (0.50 to 9.00 cm) is varied according to the expected heat load. The gaps can locally disrupt the external boundary layer and are, therefore, sources for high localized heating during entry into the Earth's atmosphere.

Past experimental studies (refs. 1 to 3) have identified as a potential problem high localized heating regions on RSI tiles where the flow in a longitudinal gap intersects a transverse gap and impinges on a downstream blocking tile. The intensity of the localized heating is influenced by tile and gap geometries, local flow conditions, and tile orientation to the direction of flow. However, these studies did not address the localized heating regions in sufficient detail to permit accurate assessment of the overall impact of this impingement heating at the downstream blocking tile. Therefore, an experimental heat-transfer investigation was conducted to define the heating distribution in the impingement region and to determine the influence of tile and gap geometries in sufficient detail to develop empirical relationships for impingement heating in laminar and turbulent boundary layers.

This study was carried out using metallic tiles in staggered arrays. The test parameters were longitudinal gap length, gap width, slope of the forward-facing walls, boundary-layer thickness and state (laminar/turbulent), and Reynolds number. The tiles were densely instrumented in areas of expected high heating to obtain well-defined impingement heating distributions. The cold-wall heating rates were obtained in the Langley 8-foot high-temperature structures tunnel at a nominal Mach number of 7, a nominal total temperature of 1800 K, free-stream unit Reynolds numbers from 1.0×10^6 to 4.8×10^6 per m, and a free-stream dynamic pressure range of 15 to 61 kPa.

SYMBOLS

The units used for the physical quantities in this paper are given in the International System of Units (SI). U.S. Customary Units were used for the principal measurements and calculations.

c_p	specific heat, J/kg-K
d	total tile thickness, cm
dT/dt	temperature rise rate, K/s

L	length of longitudinal gap (fig. 3), cm
l	total length of calibration panel (fig. 11), cm
$P_{t,c}$	total pressure in combustor, MPa
p	pressure, MPa
q	dynamic pressure, kPa
\dot{q}	cold-wall heating rate, kW/m ²
R	unit Reynolds number, per m
R_l	local Reynolds number based on distance from panel holder leading edge
$R_{l,L}$	local Reynolds number based on gap length
s	surface distance from tile radius mid arc, cm
$T_{t,c}$	total temperature in combustor, K
W	gap width (fig. 3), cm
x	distance from leading edges of calibration panel (fig. 11), cm
z	vertical distance into gap (fig. 2), cm
α	angle of attack, deg
δ^*	boundary-layer displacement thickness, cm
θ	slope of forward-facing wall (fig. 3), deg
θ_{rad}	slope of forward-facing wall, rad
ρ	density, kg/m ³
τ	material thickness, cm
ϕ	theoretical heating-rate ratio

Subscripts:

atm	atmospheric
e	experimental
em	empirical
FP	flat-plate condition

I impingement
S surface

TEST APPARATUS

Model Description

Calibration panel.- As shown in figure 1, the calibration panel was instrumented with 35 number 30-gage chromel-alumel thermocouples which were spot welded to the back surface of a 0.05-cm-thick 304 stainless-steel plate. (See ref. 1 for further details.) The calibration panel was used to determine tunnel operating parameters which would yield a laminar boundary layer over the test panels and to obtain the corresponding cold-wall laminar heating rates for reference data.

Tile array panels.- The tile arrays shown in figure 2 were nominally 46 by 48 by 6.35 cm and consisted of solid aluminum tiles surrounding two instrumented stainless-steel thin-wall (0.08 cm) tiles. Metallic tiles were used to simulate the RSI tiles because they were easier to handle, and the tile material has no effect on the cold-wall heating rates. Each tile had an edge radius of 0.25 cm. The model schematics indicate orientation to the flow direction, instrumented tile locations, and geometric parameters. The geometric parameters listed are longitudinal gap length L , gap width W , and slope of the forward-facing wall θ . The test ranges of these parameters are compared with the nominal shuttle geometric parameters in figure 2(c). The forward-facing walls of the thin-walled tiles are sloped at 60° , 75° , or 90° . For convenience, the 60° and 75° walls were provided on the same tile (figs. 2(a) and 2(b)) and required only 180° rotation and appropriate filler bars to change configurations. All the tiles were mounted on a 0.32-cm-thick stainless-steel plate with slotted holes to permit adjustment of tile position to change gap width. The gap widths were 0.10, 0.18, 0.30, and 0.41 cm. Longitudinal gap lengths were 15.24 and 30.48 cm. Photographs of the models are shown in figure 3.

The thin-wall tiles were instrumented with 30-gage chromel-alumel thermocouples spot welded to the inside surface of the tiles. The thermocouples were distributed both longitudinally and laterally over the tile surface as shown in figures 4 and 5. Thermocouples are concentrated in the impingement regions at the downstream end of the longitudinal gap to define the expected highly nonuniform heating distributions. Each $60^\circ/75^\circ$ tile had 43 thermocouples and each 90° tile had 25 thermocouples. The numbers in the figures indicate thermocouple designations for tiles at the end of the 15.24-cm longitudinal gap. Thermocouple designations for $L = 30.48$ cm may be obtained by adding or subtracting the constants indicated in the respective figures.

In order to define heating distributions in the impingement region, precise thermocouple locations had to be known. The thermocouple locations were precisely determined by using optical measurement equipment and radiographs of the thin-wall tiles to identify the mean longitudinal center line of the thermocouples. These thermocouples varied within ± 0.03 cm of the scribed mean longitudinal center line. A precision alignment rig was used to align the mean ther-

couple center line with the upstream longitudinal gap center line and to set the desired gap widths.

Panel Holder

The models were mounted in a panel holder (figs. 6 and 7) which can accommodate test panels up to 152 by 108 cm. (See refs. 4 and 5.) The aerodynamic surface is covered with 1.25-cm-thick low conductivity Glasrock tiles. Aerodynamic fences (fig. 6) provide uniform two-dimensional flow over the entire aerodynamic surface. A blunt leading edge with a radius of 0.95 cm is used on the panel holder to promote a laminar boundary layer, and a sharp leading edge with a lateral row of boundary-layer trips is used to promote a turbulent boundary layer over the aerodynamic surface of the panel holder. Two test locations were provided in the panel holder 117 and 188 cm from the leading edge. The calibration panel and the 60°/75° sloping tile array were located in the forward location (location I), and the 90° tile array was located in the rear location (location II).

Facility

The tests were performed in the Langley 8-foot high-temperature structures tunnel (fig. 8) which is a large blowdown facility that simulates aerodynamic heating and pressure loading at a nominal Mach number of 7 and an altitude between 25 and 40 km. The high energy needed for this simulation is obtained by burning a mixture of methane and air under pressure in the combustor and expanding the products of combustion through a conical-contoured nozzle into the open jet test chamber. The flow enters a supersonic diffuser where an air ejector pumps the flow through a mixing tube and exhausts the flow to the atmosphere through a subsonic diffuser. This tunnel operates at a combustor total temperature $T_{t,c}$ between 1400 and 2000 K and combustor total pressures $P_{t,c}$ from 4.1 to 24.1 MPa. Free-stream unit Reynolds numbers range from 1.0×10^6 to 10.0×10^6 per m.

Test models are mounted on an elevator and inserted into the test stream after the test conditions are established to avoid exposing test models to tunnel transients which occur during tunnel start-up and shutdown. A model pitch system provides an angle-of-attack range of $\pm 20^\circ$. More detailed information can be found in references 4 and 5.

TESTS

Wind-tunnel tests were made on a calibration panel and on tile array panels. The calibration panel was used to determine tunnel flow conditions which would yield a laminar boundary layer over the test panels. The calibration panel was also used to obtain corresponding cold-wall laminar heating rates for data correlation with nonsmooth surfaces. The tile array panels were used to define the heating distribution in the impingement region and to determine the

influence of tile and gap geometries in sufficient detail to develop empirical relationships for impingement heating in laminar and turbulent boundary layers.

Test Procedures and Data Reduction

The test procedures were to establish the tunnel equilibrium flow conditions and then insert the model into the test stream. The model was pitched during insertion to the desired angle of attack to give it, as nearly as possible, a step-function exposure to the test condition. A typical insertion history showing the model position, the angle of attack, and a typical temperature response on the metallic tiles is shown in figure 9. The model traverses 210 cm to the tunnel center line in a little over 2 s. The panel holder reaches the desired angle of attack at approximately 1 s after insertion. The tile temperature response shows that the maximum temperature rise rate occurs before the model reaches the tunnel center line. However, until the model reaches the tunnel center line, the entire panel holder is not exposed to a uniform test environment. Therefore, the time of data analysis, as shown in figure 9, was chosen as the time when the model reached the tunnel center line.

Models and tunnel instrumentation data were recorded by high-speed digital recorders at 20 and 200 frames per s. Cold-wall heating rates were calculated from these outputs using the one-dimensional transient heat balance equation ($\dot{q} = \rho c_p \tau (dT/dt)$). The temperature rise rate dT/dt was calculated by averaging the model temperatures over 0.25-s intervals and then determining the temperature rise rate between each interval. Therefore, the heating rates were determined each 0.25 s.

The one-dimensional heat balance equation equates the convective energy entering the surface to the energy stored and does not consider the effect of conduction and radiation. These assumptions are considered reasonable since the temperature-time slopes were taken early in the tests when the surface temperatures were relatively low. In addition, calculations made to account for conduction and radiation effects indicated these heat losses were less than 2 percent at the time data were taken.

Conditions

The tunnel conditions for the calibration series are given in table I. The calibration panel was tested three times in nominal tunnel conditions of $T_{t,c} = 1800$ K, dynamic pressures of 14 and 42 kPa, free-stream unit Reynolds numbers of 1.0×10^6 and 3.0×10^6 per m, and $\alpha = 0^\circ$ and 4.5° . The three selected combinations of these tunnel conditions resulted in laminar flow over the calibration panel.

Tunnel conditions and test parameters for the tile array models are given in table II. The tile arrays were tested a total of 17 times; 7 tests were made in a laminar boundary layer and 10 in a turbulent boundary layer. The laminar tests were at $T_{t,c} = 1800$ K (nominal), dynamic pressures of 15 and 32 kPa, free-stream unit Reynolds numbers of 1.0×10^6 and 2.6×10^6 per m, and $\alpha = 0^\circ$. The turbulent boundary-layer tests were at $T_{t,c} = 1800$ K (nominal),

dynamic pressures of 25 and 61 kPa, free-stream unit Reynolds numbers of 2.0×10^6 and 4.0×10^6 per m, and $\alpha = 0^\circ$ and 7.5° . These conditions yielded laminar δ^* values of 0.36 and 0.57 cm and turbulent δ^* values between 0.85 and 1.62 cm (ref. 6). The free-stream tunnel conditions were determined from temperatures and pressures measured in the combustor and are based on the thermal, transport, and flow properties of methane-air combustion products as reported in reference 7 and in the tunnel surveys of reference 5.

RESULTS AND DISCUSSION

Flow Conditions and Test Data

Calibration test data.- Typical experimental cold-wall convective heating rate distributions over the calibration panels are compared with theory in figure 10 for laminar and turbulent boundary layers. The laminar data were obtained on the calibration panel in the forward region of the panel holder. (See inserts in fig. 10(a).) The turbulent data were obtained from an earlier study using a large calibration panel (ref. 5) which covered the entire test area of the panel holder. A sharp leading edge with a lateral row of spherical boundary-layer trips (see inserts in fig. 10(b)) was used to promote turbulence. The theoretical predictions shown by the dashed curves were calculated using equations and plots from reference 5. In general, the laminar boundary-layer theory was 10 percent higher than the laminar experimental data (fig. 10(a)) obtained on the small calibration panel. Reference 5 reported turbulent boundary-layer theory to be approximately 30 percent higher than the interpolated experimental data (fig. 10(b)) which was an expected error. The interpolated experimental data were obtained by interpolating between data in reference 5.

Laminar flow conditions existed over location I for the range of test conditions listed in table I. Flat-plate heating rates in laminar flow range between 6.5 and 9.0 kW/m². Results from reference 5 showed that uniform turbulent flow could be maintained over the entire test surface of the panel holder for test conditions of $6.8 \text{ MPa} \leq p_{t,c} \leq 17.3 \text{ MPa}$ and $0^\circ \leq \alpha \leq 15^\circ$. The flat-plate heating rates in turbulent flow range between 63 and 137 kW/m².

Tile array test data.- Experimental tile heating rates nondimensionalized by flat-plate heating rates are tabulated in table III for each thermocouple location. Flat-plate heating rates \dot{q}_{fp} in a laminar boundary layer were obtained on the small calibration panel at the location of the thin-wall tile centers except for the condition $p_{t,c} = 10.2 \text{ MPa}$ and $\alpha = 0.3^\circ$. At this test condition the theoretical value of the \dot{q}_{fp} was used because calibration data were not available. This theoretical value is considered to be reliable because of the good agreement between experiment and theory shown in figure 10(a). As previously mentioned, the flat-plate heating rates in a turbulent boundary layer were obtained from the experimental data of reference 5 at the location of the thin-wall tile centers.

Under certain flow conditions the presence of the tile array (location I) appeared to create transitional flow where laminar flow existed over the calibration panel. For example, whereas laminar heating rates were obtained on the

smooth calibration panel at $P_{t,c} = 4.0$ MPa and $\alpha = 4.5^\circ$ (see table I), heating rates indicative of transition were obtained on the tile array at the same test conditions and location. This phenomenon was also noted in reference 8. Heating rate data for location II were indicative of transitional flow at all flow conditions with the arrays present. (In general for the flow conditions presented, ref. 5 indicated laminar flow for a smooth surface.) No laminar heating rate data were obtained for the tile array in location II. Tunnel conditions, test parameters (table II), and heating rate ratios (table III) are tabulated only for runs where the boundary layer was either laminar or turbulent.

Aerodynamic Heating in Laminar Flow

Tests were conducted under laminar flow conditions to identify local flow characteristics and to determine the magnitude and distributions of the convective heating in the impingement region downstream of a longitudinal gap as affected by changes in gap geometries. All the laminar data plotted are for test conditions of $P_{t,c} = 4.3$ MPa, $\alpha \approx 0^\circ$, $\delta^* = 0.57$ cm, and $\theta = 60^\circ$ and 75° .

Heating rate distributions in impingement region.— Typical laminar convective heating rate distributions along the longitudinal center line of the thin-wall tiles ($L = 15.24$ cm) are shown in figure 11 for $W = 0.18$ and 0.41 cm. The local heating rate is nondimensionalized by the flat-plate heating rate. The forward-facing walls of the tiles have been rotated up in the sketches for clarity in the plots. Thermocouple numbers in the sketches correspond to those in figure 4. The heating rate distributions in figure 11 show that the impingement region heating rates increase with increasing W and θ . Peak heating at all gap widths occurs on the top surface near the edge radius of the tiles, and the maximum heating rate ratio is 2.2. Results for gap widths of 0.10 and 0.30 cm follow the same trends.

The heating rate distributions down the forward face for all tile array configurations with $L = 15.24$ cm are shown in figure 12. Locations of the thermocouples are shown in the inserts. In all cases the heating decreases significantly with increasing depth into the gap. In fact, the maximum heating rate was only $0.1\dot{q}_{fp}$ at 30 percent of the tile depth. Data shown for $\dot{q}/\dot{q}_{fp} < 0.02$ are of questionable accuracy because of limitations in the data recording system. By integrating the center-line heating distribution on the forward-facing tile wall, the heat load per unit width is shown to decrease with decreasing θ for $W = 0.18$ cm even though the surface area increases. The percent decrease in the impingement heating rate and in the heat load per unit width obtained by decreasing θ from 75° to 60° is 31 percent and 56 percent, respectively, for $W = 0.18$ cm. Very little decrease is shown for $W = 0.41$ cm.

Details of the heating in the impingement regions are shown in figure 13 for forward-facing wall slopes of 60° and 75° with gap widths of 0.18 and 0.41 cm (longitudinal gap length is 15.24 cm). The short-dashed lines represent outlines of the upstream gap, and the long-dashed lines represent tangencies between the edge radius and top and forward-facing tile surfaces. Here the basic flow phenomenon created by longitudinal and transverse gaps is characterized by isomet-

ric heating rate contours. As these contours were generated, the heating rates were assumed to be symmetric about the mean thermocouple center line.

The uniformity of the heating rates in the transverse direction for $W = 0.18$ cm indicates that the gap flow is primarily two-dimensional in nature and that the longitudinal gap flow has a negligible effect on these heating rates for gap widths less than 0.18 cm. For a gap width of 0.41 cm, the contours are less uniform, which suggests that the basic flow is three-dimensional and the flow in the longitudinal gap is becoming more influential. As the gap width increases, the flow in the longitudinal gap also influences the heating on the top surfaces. Results for gap widths of 0.10 and 0.30 cm follow the same trends.

Effect of tile and gap geometry.— The effects of gap width and longitudinal gap length on surface and impingement heating rates are shown in figure 14 (\dot{q}_s obtained from thermocouple 55; \dot{q}_I obtained from thermocouple 49 or 61). Data are shown for $\theta = 60^\circ$ and 75° and the two values of gap length ($L = 15.24$ and 30.48 cm). The general trend is an increase in surface heating with an increase in W , θ , and L . This increase in surface heating caused by the presence of gaps was also noted in reference 8. The results shown in figure 13 suggest that the increased heating results from changes in flow down the longitudinal gap due to increased gap widths. The maximum increase in surface heating of $0.5\dot{q}_{FP}$ occurred at the maximum gap width ($W = 0.41$ cm). However, for the smaller gap widths the increase in surface heating is less than 10 percent. The impingement heating rate \dot{q}_I is influenced similarly by wider gaps and longer longitudinal gaps. The maximum impingement heating of $2.4\dot{q}_{FP}$ also occurs for $W = 0.41$ cm. For the two smaller gap widths, \dot{q}_I was less than the surface heating rate. The maximum increase in \dot{q}_I due to gap length for $\theta = 75^\circ$ was 60 percent and occurred for $W = 0.30$ cm; data for $\theta = 60^\circ$ indicate similar trends. As previously stated, decreasing the slope of the forward-facing wall from 75° to 60° generally decreases impingement heating and surface heating levels.

Aerodynamic Heating in Turbulent Flow

Past investigators of gap heating in a turbulent boundary layer have studied the effects of W , L , δ^* , and tile orientation. However, the effect of sloping the forward-facing wall was not investigated nor has the impingement heating region been well defined. Therefore, these effects as well as the effects of W and L were investigated for the 60° , 75° , and 90° tile arrays. Test conditions for the turbulent data plotted were $P_{t,c} = 6.8$ MPa, $\alpha = 7.5^\circ$, and $\delta^* = 1.01$, 1.36 , and 1.62 cm.

Heating rate distributions in impingement region.— Typical nondimensionalized heating rate distributions along the longitudinal center line of the tiles are shown in figure 15 for forward-facing wall slopes of 60° , 75° , and 90° . These heating rate distributions show that the heating on the forward-facing wall downstream of a longitudinal gap increases rapidly to a maximum near the edge radius, and the heating rates decrease rapidly aft of the edge radius until they reach a near uniform flat-plate value at the center of the tile. For the indicated test conditions, peak heating on the 60° and 75° forward-facing walls

is approximately 2.5 to 3.0 times the flat-plate value, whereas on the 90° walls, the heating is 4.3 times greater. However, this result depends on many other parameters discussed in later sections.

The heating distributions down the forward-facing wall for all configurations of the tile arrays with $L = 15.24$ cm are shown in figure 16. All distributions show the same general trend, a constant heating rate region at the top which decreases rapidly with gap depth. This constant heating level occurs over the upper 15 percent of the gap depth for $\theta = 90^\circ$ with $W = 0.30$ and 0.41 cm and $\theta = 75^\circ$ with $W = 0.41$ cm. For all other gap geometries the constant heating only occurs over the upper 5 percent of the gap depth. Both the maximum heating rate and the constant heating rate region increase with increases in W and θ . These trends are somewhat different from the laminar trends (fig. 12) in that the laminar results did not indicate a constant heating rate region. At all test conditions the turbulent heating has reached $0.1\dot{q}_{fp}$ or less at 60 percent of the tile depth as compared with laminar heating which reached $0.1\dot{q}_{fp}$ at 30 percent of the tile depth. As in the laminar case, integrated heat load per unit width on the forward-facing tile wall decreases with decreasing θ even though the surface area increases. The percent decrease in the heat load per unit width obtained by reducing θ from 90° to 60° and 90° to 75° with $W = 0.18$ cm is 23 percent and 10 percent, respectively.

The point of peak heating shifted slightly with changing gap width, as illustrated by the heat rate vector plots shown in figure 17. The data shown are for the 90° tile array; however, the other tile array ($\theta = 60^\circ$ and 75°) showed similar trends. For $W = 0.10$ cm the maximum heating occurred at the tangency point of the edge radius and the top surface. As W was increased, the maximum heating rate moved around the edge radius to approximately mid arc for $W = 0.18$ cm and to the tangency of the forward-facing wall and edge radius for $W = 0.30$ and 0.41 cm.

Impingement region isometric heating rate contour plots for $\theta = 60^\circ$, 75° , and 90° , at $W = 0.18$ and 0.41 cm, are shown in figure 18. The heating rates used in generating the contours were assumed to be symmetric about the mean thermocouple center line. As in figure 13, the dashed lines represent outlines of the upstream gap and the tangencies between the edge radius and top and forward-facing tile surfaces. The outlines are shown for reference only. The isometric heating rate contours indicate that the flow is three-dimensional. As was found for laminar flow, increases in W and θ cause an increase in heating intensity. The region affected by the three-dimensional flow extends at least three gap widths in the transverse and longitudinal directions. As noted previously, peak heating regions move down the tile face as gap width is increased. Results for gap widths of 0.10 and 0.30 cm follow the same trends. Peak heating rate level for all cases is greater than \dot{q}_{fp} , and a maximum heating rate ratio of 4.5 occurs for $\theta = 90^\circ$ and $W = 0.41$ cm.

Effect of tile and gap geometry.— The influence of the slope of the forward-facing wall on impingement heating is shown in figure 19 where the impingement heating rate (\dot{q}_I obtained from thermocouple 49, 61, or 93) nondimensionalized by the flat-plate heating rate value is plotted against the forward-facing wall slope θ . Data are plotted for $\delta^* = 1.01$ cm at $\theta = 60^\circ$ or 75° , and for $\delta^* = 1.36$ cm at $\theta = 90^\circ$. (No data were taken on the 90° tile array for

$\delta^* = 1.01$ cm.) Experimental data (ref. 1) indicate that heating decreases with increases in δ^* ; consequently, heating rates for $\theta = 90^\circ$ at $\delta^* = 1.01$ cm would be greater than heating rates shown for $\delta^* = 1.36$ cm. The 60° and 75° data indicate that θ significantly influences impingement heating. There is insufficient data to show details of the trend from 60° to 90° ; however, the influence of θ can be considered analytically and is discussed in a later section.

The effects of gap width and longitudinal gap length on impingement heating rate are shown in figure 20. As noted previously, the impingement heating rate increases with gap width and the slope of the forward-facing tile wall; the effect of longitudinal gap length is not as obvious. For the longer length gap and $\theta = 60^\circ$ (open squares, fig. 20(a)), increasing the gap width causes the impingement heating rate first to decrease and then to increase (at $W > 0.18$ cm) to levels that can be greater than the corresponding heating rate level for the shorter gap (open circles). The data for $\theta = 75^\circ$ (solid symbols, fig. 20(a)) appear to substantiate the trends noted above for $\theta = 60^\circ$; however, for $\theta = 90^\circ$ the impingement heating rate for the longer length gap does not increase to levels higher than the corresponding levels for the shorter length gap. This inconsistency with data at $\theta = 60^\circ$ and 75° is not fully understood because of limited data; however, the inconsistency may be attributed to the thicker boundary layer which is the only difference in the data. Unpublished results from tests at NASA Langley and Ames Research Centers indicate that a periodic heating pattern exists along the length of longitudinal gaps (gap lengths were 15, 48, and 84 cm with gap widths up to 0.48 cm). The fluctuations in the impingement heating rate indicated in figure 20 may be due to the same unexplained phenomenon noted in the longitudinal gaps.

Geometric effects of θ , W , and L on the midpoint surface heating rates are indicated in figure 21. The geometric parameters have an overall opposite effect on surface heating than on impingement heating; that is, if a change in a parameter tends to increase the impingement heating, then that change tends to decrease the surface heating. However, the same periodic heating rate effect is evident, except that the shorter longitudinal gaps also exhibit the effect. It should also be noted that the periodic surface heating rate is in phase with the periodic impingement heating (e.g., a decrease in impingement heating is accompanied by a corresponding decrease in surface heating).

Correlation of Laminar and Turbulent Data

Past investigators (ref. 9) have proposed a correlation parameter which relates heating in the impingement region with boundary-layer and tile gap geometric parameters. The authors of reference 10 extended and refined the correlation to apply to a wider range of test data. The intent was to define an impingement heating envelope for the maximum heating at any arbitrary flow and gap conditions. The correlation parameter $[(\delta^*/W)^2(z/L)]$ relates the impingement heating rate to boundary-layer displacement thickness δ^* , gap width W , data point vertical location z , and longitudinal gap length L . This correlation parameter does not adequately correlate the laminar data. Therefore, the parameter was modified to include laminar data by including a ratio ϕ^6 where ϕ is the ratio of the theoretical heating rate for turbulent flow divided by

the theoretical heating rate for the actual flow conditions over a smooth surface. (The ratio equals one when the actual flow is turbulent and is greater than one when the actual flow is laminar.) The present data and turbulent flow data from references 1 and 9 plotted against the modified correlation parameter are compared with the upper bound for impingement heating from reference 10 in figure 22. The correlation parameter gives only fair agreement with experimental data and does not identify all the governing parameters and their degree of influence. Consequently, empirical relationships were developed which could accurately predict the maximum impingement heating as well as indicate the governing parameters and their degree of influence.

The experimental data presented herein indicate that impingement heating is dependent on governing parameters of gap geometry (W , L , and θ) and flow conditions (boundary-layer thickness and Reynolds number). Even though data from references 1 and 9 were included in the data base to enlarge the parameter range, sufficient data were not available to isolate the independent effects of all the parameters. This deficiency can be bridged by using a regression analysis. The regression analysis method of references 11 and 12 was used to investigate many functional relationships between the heating rate data and the flow and geometric parameters.

An equation of the general form

$$y = a_0 x_1^{a_1} x_2^{a_2} x_3^{a_3} \dots \quad (1)$$

was found to yield the "best fit" to the data. By studying the experimental data, the physical problem, and the computed statistical information about each parameter and functional relationship, parameters having a significant influence on the impingement heating rates could be determined. The following table shows all the parameters investigated and the parameters that were found to exert the most significant influence on the impingement heating rates:

Boundary-layer state	Parameters investigated	Parameters of significant influence
Laminar	δ^* , δ^{*2} , W , W^2 , δ^*/W , $(\delta^*/W)^2$, z , W/δ^*z , $(W/\delta^*z)^2$, $(W/\delta^*z)^3$, $(W/\delta^*z)^{0.5}$, L , z/L , ϕ , $\ln \phi$, R_L , R_l , $R_{l,L}$, $\sin \theta$, θ_{rad}	δ^*/W , $R_{l,L}$, R_l , $\sin \theta$
Turbulent	δ^* , δ^{*2} , W , W^2 , δ^*/W , $(\delta^*/W)^2$, z , W/δ^*z , $(W/\delta^*z)^2$, $(W/\delta^*z)^3$, $(W/\delta^*z)^{0.5}$, L , z/L , ϕ , $\ln \phi$, R_L , R_l , $R_{l,L}$, $\sin \theta$, θ_{rad} , PS/P_{atm}	δ^*/W , PS/P_{atm} , $R_{l,L}$, $\sin \theta$

For a laminar boundary-layer state, all the expected governing flow and geometric parameters had a significant influence. Some of the parameters are interrelated (e.g., δ^*/W and $R_{l,L}$) indicating an interaction between the flow and

geometric parameters. The functional relationship of θ could not be adequately defined as an independent parameter. Consequently, the effect of θ was qualitatively taken into account by $\sin \theta$ and included with the dependent variable as $\dot{q}/\dot{q}_{FP} \sin \theta$. For a turbulent boundary-layer state the same governing flow and geometric parameters were found to be influential except for R_l . As in the laminar case, R_l was expected to be an influential parameter; however, turbulent data correlated better using the surface pressure p_s . Although there is a direct relationship between p_s and R_l , the latter parameter also reflects changes in other parameters (e.g., velocity for the present tests); in addition the turbulent gap flow phenomenon is apparently better characterized by the surface pressure p_s .

In obtaining the regression equation, all data were initially input into the regression analysis, and those observations with high residuals were then eliminated to improve the overall fit (for laminar flow, 10 of 14 observations were retained; for turbulent flow, 27 of 51 observations were retained). The final data used in obtaining the regression equations are listed in table IV. The observation number for each of the first 30 observations indicates the run number (first two digits) and the thermocouple number (last three digits) for the present data. The resulting regression equations are as follows:

$$\text{Laminar: } \frac{\dot{q}}{\dot{q}_{FP} \sin \theta} = 17\,000 \left(\frac{\delta^*}{W} \right)^{-1.12} R_{l,L}^{-0.07} R_l^{-0.53} \quad (2)$$

$$\text{Turbulent: } \frac{\dot{q}}{\dot{q}_{FP} \sin \theta} = 5.58 \left(\frac{\delta^*}{W} \right)^{-0.44} R_{l,L}^{+0.05} \left(\frac{p_s}{p_{atm}} \right)^{0.18} \quad (3)$$

These equations were then compared with the test data to assess their adequacy in predicting the impingement heating level and the influence of the governing parameters. The equation for turbulent flow did not fully account for the effects of gap width and slope of the forward-facing wall. Therefore, the regression equation (eq. (3)) was used as the basis to graphically isolate the effects of W and θ . This combined regression analysis and graphic technique resulted in the following equation:

$$\frac{\dot{q}}{(\dot{q}_{FP})_{EM}} = 5.58 \left(\frac{\delta^*}{W} \right)^{-0.44} R_{l,L}^{0.05} \left(\frac{p_s}{p_{atm}} \right)^{0.18} (-0.43W + 0.47e^{0.70 \theta \text{ rad}}) \quad (4)$$

The form of the additional terms in equation (4), which resulted from the graphic technique, was inconsistent with the form requirement of the regression analysis technique. (See eq. (1).) The adequacy of the combined equation (eq. (4)) is illustrated in figure 23. The regression equation for turbulent

flow (eq. (3)) does not predict the heating levels for the effects of θ and W (fig. 23(a)); however, the combined equation (eq. (4)) accurately predicts both the trend and levels. The data indicate a reduction in heating of approximately 32 percent when reducing θ from 90° to 60° ; however, equation (4) indicates that a reduction in heating of 38 percent may be possible. The combined equation also improved predictions for the effect of W as shown in figure 24(b).

The accuracy of these empirical relationships (eqs. (2) and (4)) is illustrated in figure 24. Ninety percent of the laminar and turbulent impingement heating rates can be predicted within ± 29 percent. Consequently, equations (2) and (4) accurately predict the impingement heating rate and the influence of gap flow and geometric parameters within the data range used to develop the relationships.

CONCLUDING REMARKS

An experimental heat transfer investigation was conducted using metallic tiles arranged in two staggered tile arrays with longitudinal and transverse gaps between the tiles. This tile arrangement results in longitudinal gaps terminating at intersections with transverse gaps which creates a direct impingement of the longitudinal gap flow on the forward face of a downstream blocking tile; hence, high localized heating occurs at this impingement region. The tile arrays were tested to define the impingement heating distribution on a downstream blocking tile and to determine the influence of tile and gap geometries in sufficient detail to develop empirical relationships for impingement heating in laminar and turbulent boundary layers. The tests were conducted in the Langley 8-foot high-temperature structures tunnel at a nominal Mach number of 7, a nominal total temperature of 1800 K, and free-stream unit Reynolds numbers from 1.0×10^6 to 4.8×10^6 per m. Tile forward-facing wall slopes of 60° , 75° , and 90° were tested along with longitudinal gap lengths of 15.24 and 30.48 cm and gap widths of 0.10, 0.18, 0.30, and 0.41 cm. The boundary-layer displacement thickness covered a range from 0.36 to 1.62 cm. No laminar data were obtained on the 90° tile array.

For laminar boundary layers, the heating rates observed on the downstream blocking tile in the transverse gap direction for a gap width of 0.18 cm indicate that the gap flow is primarily two-dimensional in nature (i.e., flow in the longitudinal gap does not turn and flow in a transverse gap). Thus, the longitudinal gap flow has a negligible effect on the heating rates on the blocking tile for gap widths less than 0.18 cm. For a gap width of 0.41 cm the isometric heating rate contours are less uniform and suggest that the basic flow is three-dimensional; thus, the flow in the longitudinal gap is becoming more influential. The data indicate that the maximum impingement heating rate of 2.4 times the flat-plate heating rate occurs for a gap width of 0.41 cm, whereas for the two smaller gap widths, the impingement heating was less than the surface heating. As the gap width increases, the flow in the longitudinal gap also influences the heating on the top surfaces. In addition, decreasing the slope of the forward-facing wall from 75° to 60° moderately decreases the impingement heating level and surface heating.

For turbulent boundary layers, the transverse flow is primarily three-dimensional in nature. The region affected by the three-dimensional flow extends at least three gap widths in the transverse and longitudinal directions. A maximum heating rate ratio of 4.5 occurs for a forward-facing wall slope of 90° and a gap width of 0.41 cm. The impingement heating generally increases with increases in gap width, gap length, and slope of the forward-facing tile wall. However, the effects of gap width and gap length are not completely understood because a combination of factors apparently creates a periodic fluctuation in the impingement heating for long gaps. In contrast, the geometric parameters have an overall opposite effect on heating of the surface of the tile immediately downstream of the impingement region; that is, if the parameter tends to increase impingement heating, the parameter tends to decrease the surface heating. The same periodic heating rate effect observed in the impingement region is evident on the top surface and occurred for both long and short gaps. Impingement heating rates can be reduced as much as 38 percent when the forward-facing wall slope is reduced from 90° to 60° . In addition, the integrated heat load per unit width on the forward face is correspondingly decreased 23 percent even though the surface area is increased.

Empirical relationships to correlate impingement heating with gap flow and geometric parameters for laminar and turbulent flow were developed through combined regression analysis and graphic techniques. These relationships accurately predict the impingement heating rate and the influence of gap flow and geometric parameters within the data range used to develop the relationships. Ninety percent of the impingement heating rates can be predicted within ± 29 percent.

Langley Research Center
National Aeronautics and Space Administration
Hampton, VA 23665
May 26, 1978

REFERENCES

1. Weinstein, Irving; Avery, Don E.; and Chapman, Andrew J.: Aerodynamic Heating to the Gaps and Surfaces of Simulated Reusable-Surface-Insulation Tile Arrays in Turbulent Flow at Mach 6.6. NASA TM X-3225, 1975.
2. Hunt, L. Roane; Shideler, John L.; and Weinstein, Irving: Performance of LI-1542 Reusable Surface Insulation System in a Hypersonic Stream. NASA TN D-8150, 1976.
3. Brewer, R. A.; Saydah, A. R.; Nestler, D. E.; and Florence, D. E.: Thermal Performance Evaluation of RSI Panel Gaps for Space Shuttle Orbiter. J. Spacecraft & Rockets, vol. 10, no. 1, Jan. 1973, pp. 23-28.
4. Deveikis, William D.; Bruce, Walter E., Jr.; and Karns, John R.: Techniques for Aerothermal Tests of Large, Flightweight Thermal Protection Panels in a Mach 7 Wind Tunnel. NASA TM X-71983, 1974.
5. Deveikis, William D.; and Hunt, L. Roane: Loading and Heating of a Large Flat Plate at Mach 7 in the Langley 8-Foot High-Temperature Structures Tunnel. NASA TN D-7275, 1973.
6. Maslowe, S. A.; and Benson, J. L.: Computer Program for the Design and Analysis of Hypersonic Inlets - Final Report. Rep. No. 18079 (Contract No. NAS 2-1460), Lockheed-California Co., Aug. 31, 1964. (Available as NASA CR-77749.)
7. Leyhe, E. W.; and Howell, R. R.: Calculation Procedure for Thermodynamic, Transport, and Flow Properties of the Combustion Products of a Hydrocarbon Fuel Mixture Burned in Air With Results for Ethylene-Air and Methane-Air Mixtures. NASA TN D-914, 1962.
8. Christensen, H. E.; and Kipp, H. W.: Data Correlation and Analysis of Arc Tunnel and Wind Tunnel Tests of RSI Joints and Gaps. Volume I - Technical Report. NASA CR-134345, 1974.
9. Dunavant, James C.; and Throckmorton, David A.: Aerodynamic Heat Transfer to RSI Tile Surfaces and Gap Intersections. J. Spacecraft & Rockets, vol. 11, no. 6, June 1974, pp. 437-440.
10. Bohon, Herman L.; Sawyer, J. Wayne; Hunt, L. Roane; and Weinstein, Irving: Performance of Thermal Protection Systems in a Mach 7 Environment. J. Spacecraft & Rockets, vol. 12, no. 12, Dec. 1975, pp. 744-749.
11. Draper, N. R.; and Smith, H.: Applied Regression Analysis. John Wiley & Sons, Inc., c.1966.
12. Daniel, Cuthbert; Wood, Fred S.; and Gorman, John W.: Fitting Equations to Data. John Wiley & Sons, Inc., c.1971.

TABLE I.- TUNNEL CONDITIONS FOR CALIBRATION SERIES

Run number	T _{t,c} , K	P _{t,c} , MPa	q, kPa	R, per m	α, deg	Panel holder leading-edge configuration	Boundary-layer flow conditions
1	1827	4.2	14.48	1.15 × 10 ⁶	0.1	Blunt	Laminar
2	1861	4.0	13.99	1.08	4.5	Blunt	Laminar
3	1816	11.9	14.84	3.19	.1	Blunt	Laminar

TABLE II.- TUNNEL CONDITIONS AND TEST PARAMETERS FOR TILE ARRAY MODELS

Run number	$T_{t,c}$, K	$P_{t,c}$, MPa	q , kPa	R , per m	α , deg	Panel holder leading-edge configuration	Boundary-layer flow conditions ^a		θ			δ^*	
							Location I	Location II	Location I, deg	Location II, deg	W , cm	Location I, cm	Location II, cm
1	1817	4.3	15.17	1.26×10^6	0.2	Blunt	LA	TR	75	90	0.18	0.57	---
2	1863	10.2	31.92	2.55	.3						.10	.36	---
3	1910	4.2	15.72	1.12	.2						.10	.57	---
4	1723	4.3	16.13	1.10	.3						.30	.57	---
5	1867	4.3	16.00	1.31	.3						.41	.57	---
6	1840	4.2	15.10	1.14	.5						.41	.57	---
7	1780	4.2	15.37	1.29	.3						.18	.57	---
8	1867	17.2	59.01	4.26	.2						.18	1.13	1.62
9	1792	6.8	24.82	1.95	7.2						.18	1.01	1.36
10	1883	6.9	25.57	1.85	7.4						.10	1.01	1.36
11	1878	6.8	25.16	1.82	7.5						.30	1.01	1.36
12	1796	7.0	24.61	1.98	7.4						.41	1.01	1.36
13	1855	17.0	59.28	4.36	7.5						.18	.85	1.16
14	1901	17.3	60.18	4.33	.2						.18	1.13	1.62
15	1935	16.9	61.35	4.23	7.4						.18	.85	1.16
16	1707	6.8	23.58	1.98	7.6						.18	1.01	1.36
17	1742	6.9	23.71	2.07	7.6						.41	1.01	1.36

^aLA, laminar; TR, transitional; T, turbulent.

TABLE III.- HEATING RATE RATIOS ON TILE ARRAY

(a) $\theta = 60^\circ$ and $L = 15.24$ cm

Run	Boundary-layer flow conditions	\dot{q}_{pp} , kW/m ²	\dot{q}/\dot{q}_{pp} for thermocouple -																				
			44	45	46	47	48	49	50	51	52	53	54	55	67	68	69	70	77	78	79	83	84
6	Laminar	6.55	0	0.01	0.22	0.69	1.57	2.03	2.01	1.99	1.60	1.35	1.34	1.24	0.64	1.39	1.91	2.01	2.08	1.88	1.88	1.10	1.75
7	Laminar	6.55	0.02	0.02	0.07	0.29	0.55	0.66	0.84	0.88	0.86	0.90	0.94	0.07	0.26	0.62	0.64	0.24	0.49	0.77	0.24	0.49	
8	Turbulent	70.25	0	0.02	0.38	1.46	2.66	2.94	2.95	2.35	1.74	1.30	1.21	1.09	1.38	2.45	2.88	2.90	1.82	2.02	1.95	0.90	1.46
9	Turbulent	66.85	0	0.03	0.39	1.25	2.24	2.49	2.50	2.31	1.59	1.32	1.21	1.09	1.30	2.12	2.48	2.52	1.62	2.03	2.00	0.98	1.45
10		0	0	0.07	0.52	1.30	1.95	1.95	2.30	1.79	1.47	1.37	1.22	0.52	1.39	1.99	2.09	1.25	1.70	1.78	0.62	1.19	
11		0.02	0.09	0.70	1.95	2.89	3.00	3.03	2.63	1.82	1.42	1.30	1.18	0.86	2.65	2.94	2.97	2.45	2.59	2.33	1.48	1.76	
12		0.05	0.10	0.85	2.19	2.90	3.00	3.01	2.49	1.63	1.36	1.25	1.15	0.85	2.64	2.87	2.85	2.94	2.85	2.39	1.98	2.30	
13		136.98	0.02	0.08	0.66	1.40	1.85	1.96	1.94	1.81	1.40	1.16	1.12	1.04	1.49	1.83	2.02	1.96	1.53	1.73	1.68	1.00	1.42

(b) $\theta = 75^\circ$ and $L = 15.24$ cm

Run	Boundary-layer flow conditions	\dot{q}_{pp} , kW/m ²	\dot{q}/\dot{q}_{pp} for thermocouple -																				
			55	57	58	59	60	61	62	63	64	65	66	72	73	74	75	76	80	81	82	85	86
1	Laminar	6.55	1.06	1.21	1.17	1.17	0.86	0.81	0.45	0.15	0	0.03	0.02	1.22	0.86	0.75	0.45	0.20	0.22	0.80	0.45	0.95	0.53
2		9.08	1.08	1.10	0.91	0.67	0.40	0.23	0.17	0.01	0.01	0.01	0.01	0.67	0.36	0.34	0.20	0.14	0.62	0.30	0.23	0.67	0.38
3		6.55	1.07	1.11	1.12	1.08	0.77	0.60	0.44	0.15	0.04	0.12	0.02	1.06	0.62	0.46	0.37	0.08	1.00	0.71	0.35	0.79	0.48
4		6.55	1.14	1.20	1.30	1.42	1.23	1.11	0.93	0.30	0.02	0.02	0.02	1.46	1.36	1.06	0.82	0.33	1.43	1.03	0.84	0.99	0.68
5		6.55	1.39	1.47	1.82	2.03	2.07	2.06	1.71	1.02	0.17	0.03	0.01	2.07	2.06	1.96	1.70	0.88	1.99	1.92	1.47	0.88	1.28
14	Turbulent	70.25	1.20	1.39	1.89	2.95	3.66	3.62	3.56	2.59	0.69	0.05	0	2.90	3.49	3.33	2.98	1.93	2.84	3.02	2.43	1.89	1.53
15		136.98	1.12	1.16	1.57	2.02	2.17	2.15	2.06	1.81	0.91	0.16	0.02	1.98	2.08	2.05	1.94	1.64	1.95	1.99	1.84	1.70	1.51
16		66.85	1.12	1.25	1.71	2.57	3.02	2.95	2.79	1.82	0.49	0.03	0	2.48	2.87	2.83	2.86	1.66	0.01	2.57	2.15	1.76	1.39
17		66.85	1.13	1.23	1.71	2.86	3.86	3.92	3.90	3.13	1.15	0.22	0.09	2.82	3.56	3.75	3.65	2.99	0	3.32	3.08	2.38	2.03

(c) $\theta = 90^\circ$ and $L = 15.24$ cm

Run ^a	Boundary-layer flow conditions	\dot{q}_{pp} , kW/m ²	\dot{q}/\dot{q}_{pp} for thermocouple -																						
			87	88	90	91	92	93	94	95	96	97	98	99	100	101	102	103	104	106	107	108	109	110	111
8	Turbulent	63.44	0	0.05	2.44	3.21	4.06	4.26	3.86	2.75	1.54	1.03	0.87	0.89	2.06	3.14	3.97	4.07	3.63	1.93	2.79	3.14	2.52	1.19	1.73
9		62.99	0	0.11	2.14	2.61	3.15	3.19	3.11	2.43	1.49	1.06	0.97	0.99	1.90	2.52	3.06	3.14	3.00	1.90	2.47	2.50	2.18	1.11	1.67
10		0	0.01	0.68	1.19	1.78	2.21	2.41	2.24	1.68	1.21	1.13	1.13	0.68	1.28	1.99	2.12	2.37	1.01	1.69	2.01	2.15	0.68	1.30	
11		0.10	0.72	3.51	3.93	4.07	3.98	3.87	3.21	1.88	1.19	1.12	1.07	3.49	3.95	4.17	4.03	3.75	3.33	3.87	3.98	2.98	2.21	2.92	
12		0.07	7.52	3.67	4.09	4.35	4.13	3.79	2.82	1.70	1.10	1.02	1.02	3.58	3.98	4.20	4.23	3.63	3.59	3.98	4.05	2.87	2.37	3.13	
13		127.79	0.01	0.05	2.20	2.49	2.56	2.79	2.71	2.25	1.49	1.06	1.13	1.13	2.09	2.40	2.72	2.69	2.61	2.01	2.41	2.52	2.19	1.50	2.12
14		63.44	0.01	0.10	2.77	3.59	4.40	4.60	4.04	2.57	1.70	1.13	1.18	1.07	2.24	3.24	4.02	4.29	3.83	2.13	3.08	3.57	2.71	1.32	2.00
15		127.79	0	0.31	1.99	2.19	2.47	2.51	2.42	2.03	1.39	1.02	1.04	1.06	1.92	2.21	2.51	2.51	2.41	1.89	2.34	2.37	2.02	1.37	2.04
16		62.99	0.05	0.12	2.70	3.29	3.96	4.12	3.80	2.48	1.46	1.06	0.97	0.97	2.12	2.97	3.80	3.91	3.68	2.01	2.89	3.20	2.48	1.14	1.96
17		62.99	0.04	0.55	3.78	4.43	4.73	4.61	4.06	2.74	1.55	1.05	0.94	1.02	3.65	4.43	4.55	4.50	3.99	3.70	4.38	4.43	2.91	2.05	3.09

Discrepancies in impingement region heating between runs 9 and 16 are not understood.

TABLE III.- Concluded

(d) $\theta = 60^\circ$ and $L = 30.48$ cm

Run	Boundary-layer flow conditions	\dot{q}_{fp} , kW/m ²	\dot{q}/\dot{q}_{fp} for thermocouple -																						
			1	2	3	4	5	6	7	8	9	10	11	12	24	25	26	27	28	34	35	36	40	41	
6	Laminar	6.55	0.02	0.04	0.18	0.84	1.81	2.36	2.43	2.28	1.75	1.51	1.47	1.40	0.80	1.59	2.19	2.36	2.16	1.81	2.32	2.28	1.48	2.01	
7	Laminar	6.55	0.04	0.04	0.07	0.27	0.60	0.68	0.86	0.97	0.94	0.94	0.91	0.07	0.33	0.51	0.73	0.88	0.33	0.68	0.95	0.33	0.82		
8	Laminar	70.25	0	0.05	0.36	1.19	2.09	2.53	2.28	2.01	1.47	1.22	1.12	1.07	1.11	1.90	2.24	2.22	1.96	1.49	1.99	1.95	0.78	1.15	
9	Turbulent	66.85	0.01	0.03	0.16	0.57	1.27	2.09	2.53	2.28	1.51	1.35	1.23	1.16	1.10	0.52	1.08	1.37	1.41	1.48	0.91	1.42	1.52	0.58	1.07
10		66.85	0	0.01	0.14	0.80	1.76	2.15	2.26	2.05	1.66	1.38	1.25	1.17	0.75	1.57	2.02	2.15	1.92	1.52	2.00	1.92	0.87	1.42	
11		66.85	0.13	0.73	1.77	2.92	3.67	3.80	3.46	2.86	1.83	1.39	1.19	1.10	2.81	3.34	3.38	3.32	2.80	3.18	3.41	2.90	2.12	2.52	
12		66.85	0.08	0.63	1.83	3.00	3.53	3.45	3.36	2.78	1.77	1.33	1.13	1.06	2.95	3.40	3.34	3.34	2.78	3.24	3.20	2.76	2.28	2.60	
13		136.98	0.03	0.13	0.42	0.81	1.20	1.42	1.39	1.22	1.10	1.05	1.02	0.79	1.08	1.34	1.39	1.37	1.04	1.34	1.40	0.81	1.21		

(e) $\theta = 75^\circ$ and $L = 30.48$ cm

Run	Boundary-layer flow conditions	\dot{q}_{fp} , kW/m ²	\dot{q}/\dot{q}_{fp} for thermocouple -																					
			12	13	14	15	16	17	18	19	20	21	22	23	29	30	31	32	33	37	38	39	42	43
1	Laminar	6.55	1.08	1.10	1.05	1.15	1.21	0.97	0.73	0.46	0.13	0.02	0.01	0	1.19	0.95	0.75	0.42	0.42	1.13	0.66	0.49	0.84	0.42
2		9.08	1.42	1.20	1.22	1.21	0.99	0.59	0.49	0.27	0.26	0.04	0.10	1.20	0.72	0.48	0.45	0.34	0.88	0.46	0.48	0.67	0.40	
3		6.55	1.17	1.16	1.13	1.17	1.10	0.88	0.53	0.31	0.11	0	0.02	1.08	0.86	0.60	0.38	0.02	1.02	0.53	0.40	0.73	0.27	
4		6.55	1.29	1.34	1.24	1.63	1.79	1.90	1.66	1.39	0.66	0.07	0.01	0	1.88	1.97	1.75	1.28	0.43	1.79	1.50	1.19	1.19	0.75
5	Turbulent	6.55	1.54	1.55	1.60	1.92	2.23	2.43	2.30	2.01	1.02	0.13	0.02	0.04	2.34	2.45	2.32	2.05	0.47	2.14	1.99	1.63	1.81	1.21
14		70.25	1.20	1.25	1.32	1.70	2.13	2.89	2.85	2.63	1.63	0.44	0.07	0.01	2.26	2.98	2.93	2.64	0.01	1.96	1.94	1.62	1.31	0.90
15		136.98	1.10	1.12	1.12	1.14	1.25	1.24	1.02	0.66	0.27	0.04	0.02	0.02	1.28	1.30	1.17	1.02	0.04	1.24	1.01	0.83	1.04	0.66
16		66.85	1.14	1.19	1.20	1.25	1.45	1.54	1.18	0.48	0.05	0.01	0.002	0.002	1.50	1.63	1.51	1.19	0.04	1.35	1.01	0.72	0.89	0.42
17		66.85	1.00	1.04	1.17	1.78	2.79	4.02	4.24	4.30	4.11	2.54	1.35	0.33	3.02	4.17	4.27	4.46	0.04	2.85	3.33	3.37	2.34	2.01

(f) $\theta = 90^\circ$ and $L = 30.48$ cm

Run	Boundary-layer flow conditions	\dot{q}_{fp} , kW/m ²	\dot{q}/\dot{q}_{fp} for thermocouple -																							
			112	114	115	116	117	118	119	120	121	122	123	124	125	126	127	128	129	130	131	132	133	134	135	136
8	Turbulent	63.44	0.01	0.39	1.39	2.19	2.93	3.17	2.88	2.24	1.40	1.12	1.02	1.07	1.31	2.68	2.73	2.60	2.15	1.46	1.93	2.31	2.04	0.81	1.39	
9		62.99	0.05	0.37	1.12	1.90	2.47	2.50	2.42	2.01	1.36	1.12	1.05	1.00	1.16	1.76	2.34	2.52	2.44	2.01	1.38	1.77	2.08	1.94	0.79	1.36
10		0.08	0.07	0.83	1.61	2.28	2.39	2.48	2.34	1.65	1.34	1.25	1.21	0.72	1.39	2.25	2.39	2.41	2.30	1.74	2.19	2.14	0.76	1.36		
11		0.21	2.12	3.26	3.85	3.84	3.88	3.68	3.14	1.99	1.24	1.17	1.12	3.20	3.59	3.89	3.86	3.63	3.25	3.57	3.63	3.68	3.30	2.64	3.06	
12		0.13	2.35	3.51	4.04	3.99	3.90	3.58	3.04	1.78	1.13	1.06	1.00	3.47	3.87	4.06	4.04	3.75	3.05	3.43	3.58	3.61	3.09	2.43	3.04	
13		127.79	0.07	0.79	1.47	1.82	1.99	2.05	2.04	1.87	1.40	1.11	1.10	1.40	1.72	2.02	2.04	2.03	1.91	1.67	1.83	1.95	1.93	1.25	1.69	
14		63.44	0.02	0.37	1.49	2.35	3.15	3.17	2.93	2.33	1.62	1.24	1.22	1.15	1.38	2.00	2.85	3.08	2.86	2.33	1.49	2.00	2.53	2.22	0.81	1.40
15		127.79	0.02	0.01	1.68	2.04	2.21	2.25	2.26	2.00	1.41	1.06	1.08	1.08	1.64	1.95	2.24	2.33	2.21	2.04	1.86	2.05	2.19	2.02	1.34	1.81
16		62.99	0.02	0.37	1.30	1.97	2.66	2.77	2.59	2.01	1.30	1.09	1.05	1.00	1.19	1.67	2.43	2.75	2.55	2.03	1.32	1.88	2.30	1.99	0.67	1.39
17		62.99	0.09	2.24	3.78	4.30	4.43	4.21	3.77	2.86	1.63	1.03	0.97	1.03	3.70	4.35	4.47	4.37	5.05	2.95	3.60	4.00	3.00	2.16	2.93	

TABLE IV.- INPUT FOR REGRESSION ANALYSIS

Data source ^a	Observation number ^b	δ^* , cm	W, cm	$R_{l,L}$	R_l	P_g/P_{atm}	θ , deg	θ_{rad}	$\dot{q}/\dot{q}_{fp} \sin \theta$
Presented, LA	01018	0.57	0.18	3.62×10^5	1.93×10^6	No input	75	1.31	0.76
	01061	.57	.18	1.81	1.93		75	1.31	.84
	02018	.36	.10	8.21	4.38		75	1.31	.51
	03018	.57	.10	3.21	1.71		75	1.31	.55
	03061	.57	.10	1.61	1.71		75	1.31	.62
	04018	.57	.30	3.16	1.68		75	1.31	1.72
	05018	.57	.41	3.76	2.00		75	1.31	2.38
	05061	.57	.41	1.88	2.00		75	1.31	2.13
	06006	.57	.41	3.27	1.74		60	1.05	2.73
	07006	.57	.18	3.70	1.97		60	1.05	.69
	08006	1.13	.18	14.16	No input	0.02	60	1.05	2.92
	09049	1.01	.18	4.04		.03	60	1.05	2.88
	09117	1.36	.18	8.08		.03	90	1.57	2.47
	10006	1.01	.10	8.34		.03	60	1.05	2.48
	10049	1.01	.10	4.17		.03	60	1.05	2.25
	10092	1.36	.10	4.17		.03	90	1.57	1.78
	10117	1.36	.10	8.34		.03	90	1.57	2.28
Presented, T	11006	1.01	.30	8.34		.03	60	1.05	4.39
	11049	1.01	.30	4.17		.03	60	1.05	3.46
	11117	1.36	.30	8.34		.03	90	1.57	3.84
	12006	1.01	.41	8.80		.03	60	1.05	3.98
	12049	1.01	.41	4.40		.03	60	1.05	3.46
	12092	1.36	.41	4.40		.03	90	1.57	4.35
	13092	1.16	.18	9.53		.06	90	1.57	2.56
	15092	1.16	.18	9.72		.06	90	1.57	2.47
	16061	1.01	.18	4.24		.03	75	1.31	3.05
	16117	1.36	.18	84.86		.03	90	1.57	2.66
	17018	1.01	.41	90.40		.03	75	1.31	4.39
	17061	1.01	.41	4.52		.03	75	1.31	3.45
	17117	1.36	.41	90.40		.03	90	1.57	4.43
		12.07	.13	3.17		.002	90	1.57	.48
		12.07	.23	3.17		.002	90	1.57	.55
		1.17	.18	5.44		.03	90	1.57	2.53
		1.17	.10	4.87		.03	90	1.57	2.31
Reference 9, T Reference 9, T Reference 1, T		1.17	.30	4.97		.03	90	1.57	3.27
		1.17	.41	4.91		.03	90	1.57	3.08
		1.37	.18	6.99		.02	90	1.57	2.26

^aLA, laminar; T, turbulent.

^bxxxx: xx = Run number, yyy = Thermocouple number.

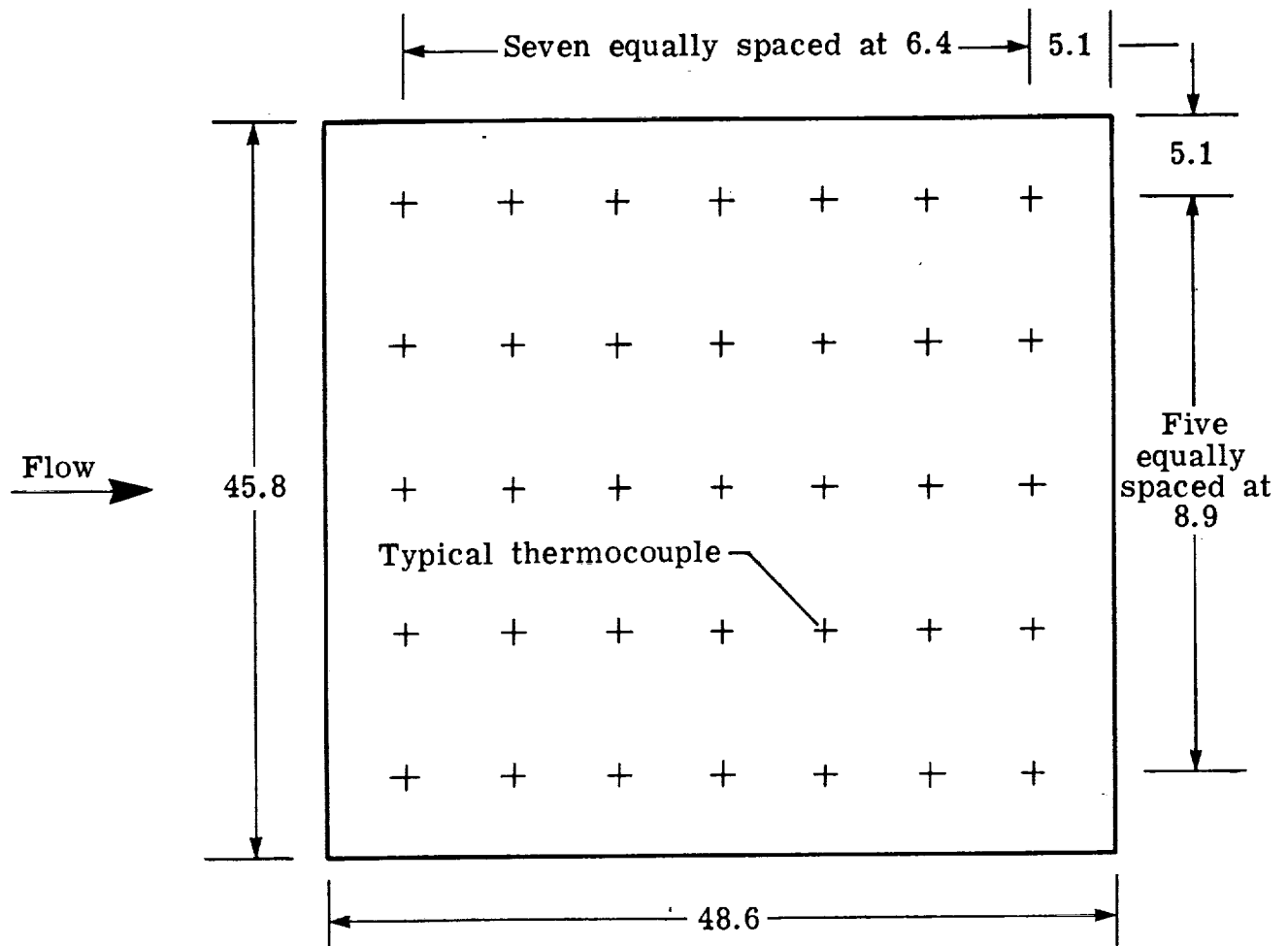
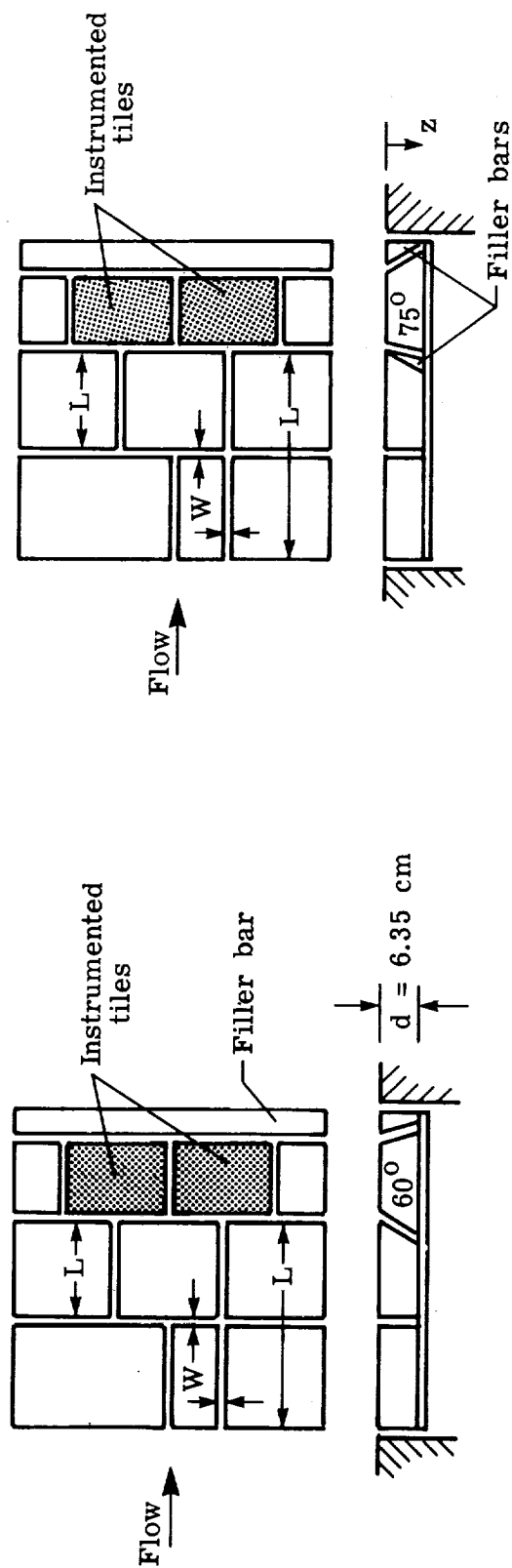


Figure 1.- Thermocouple locations on calibration panel. Dimensions are in cm.



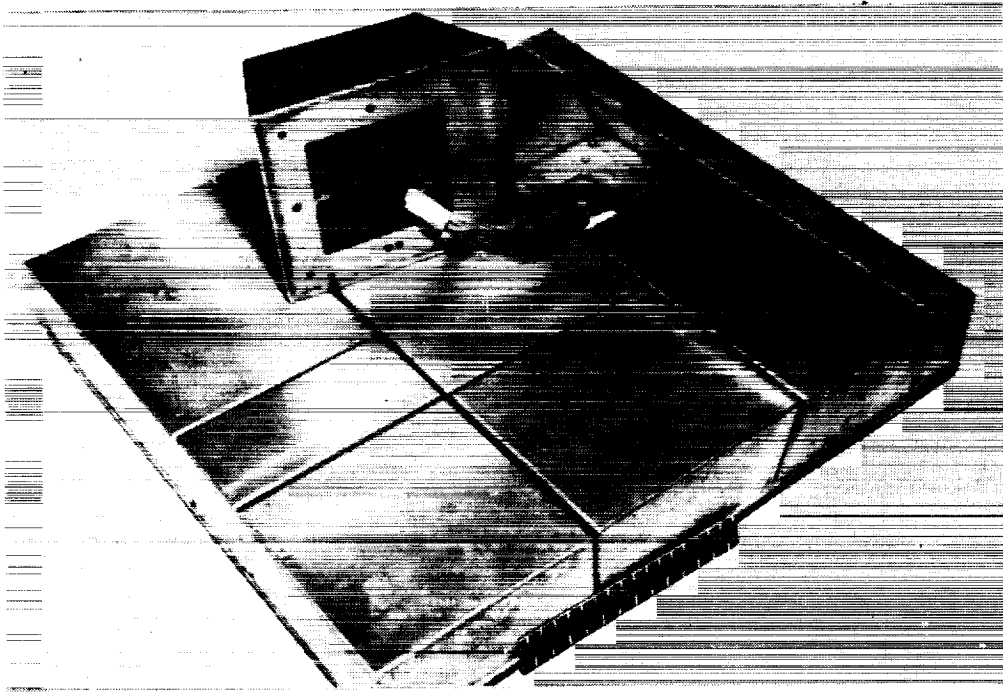
(a) $\theta = 60^\circ$.

(b) $\theta = 75^\circ$.

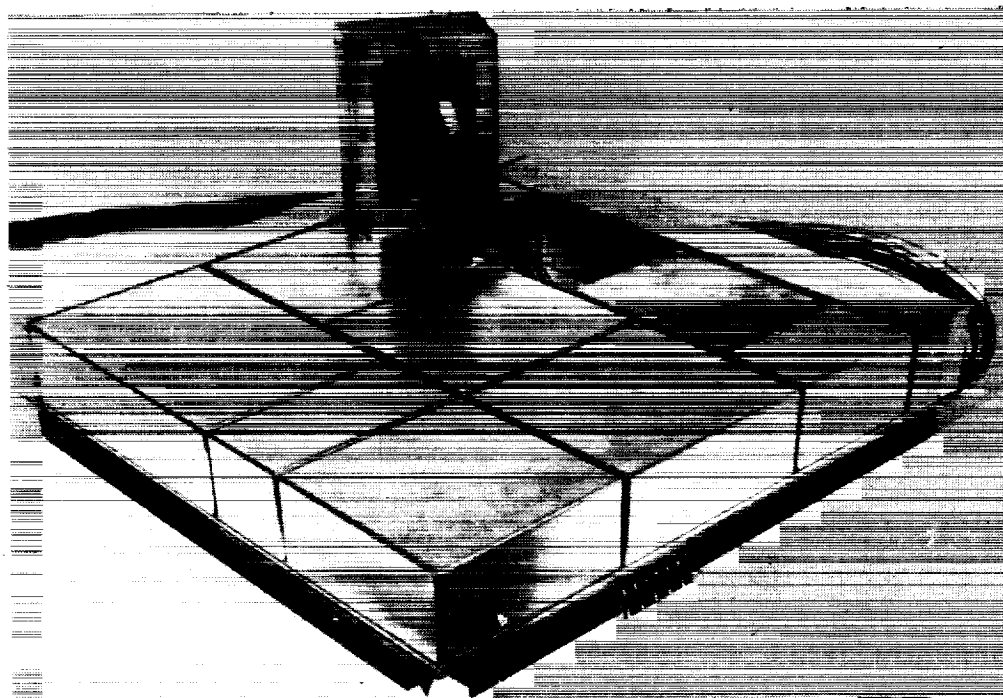
Parameters	Test range	Shuttle (nominal)
L, cm	15.24, 30.48	15.24
W, cm	0.10, 0.18, 0.30, 0.41	0.13
θ , deg	60° , 75° , 90°	90°

(c) Geometric parameters.

Figure 2.- $60^\circ/75^\circ$ metallic tile array and geometric parameters.



(a) $60^{\circ}/75^{\circ}$ tile array.



(b) 90° tile array.

L-78-104

Figure 3.- Arrays of metallic tiles.

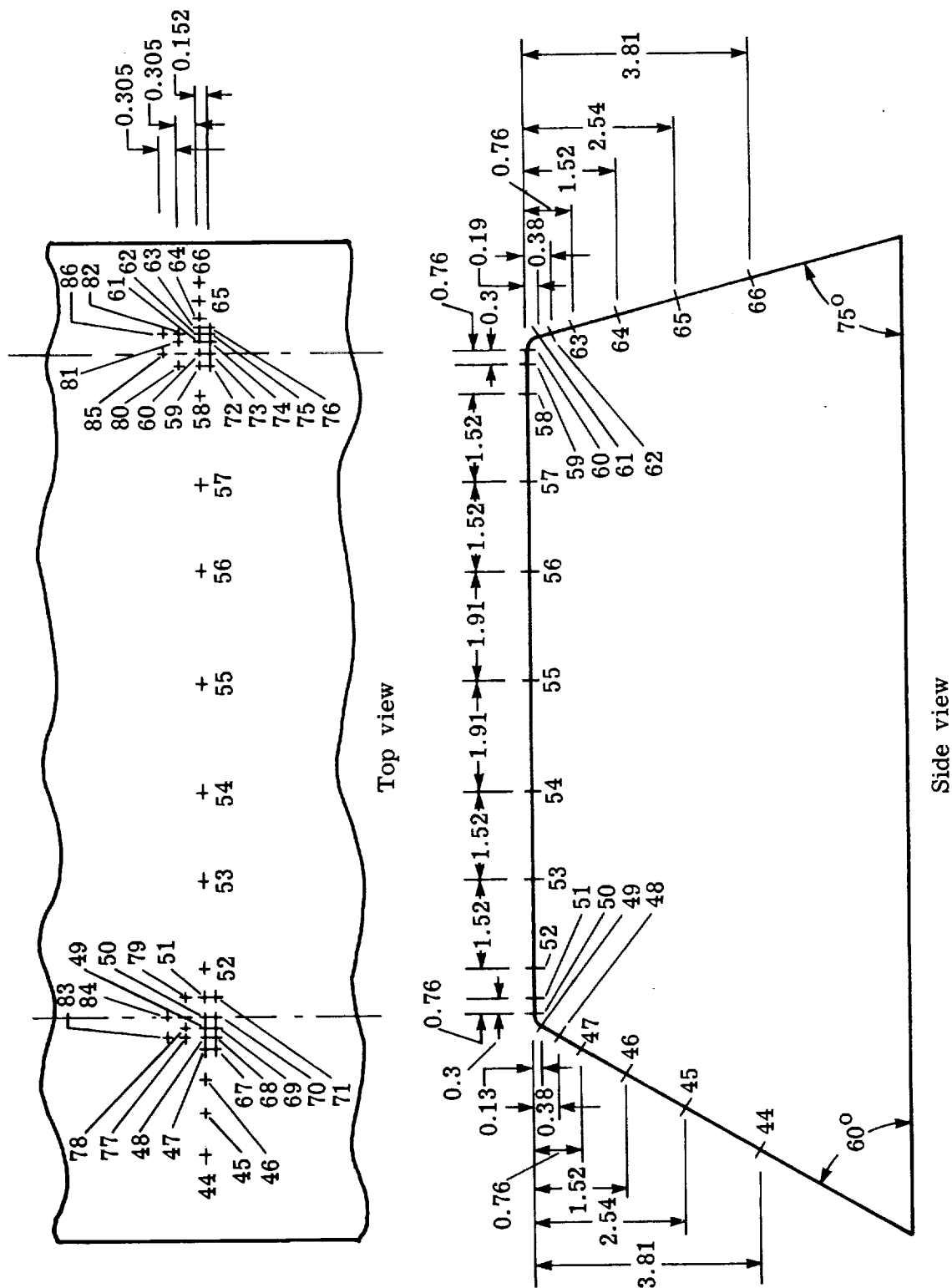


Figure 4.- Instrumentation for 60°/75° thin wall tiles. L = 15.24 cm; dimensions are in cm. (For thermocouple designation where L = 30.48 cm, subtract 43 from each thermocouple number.)

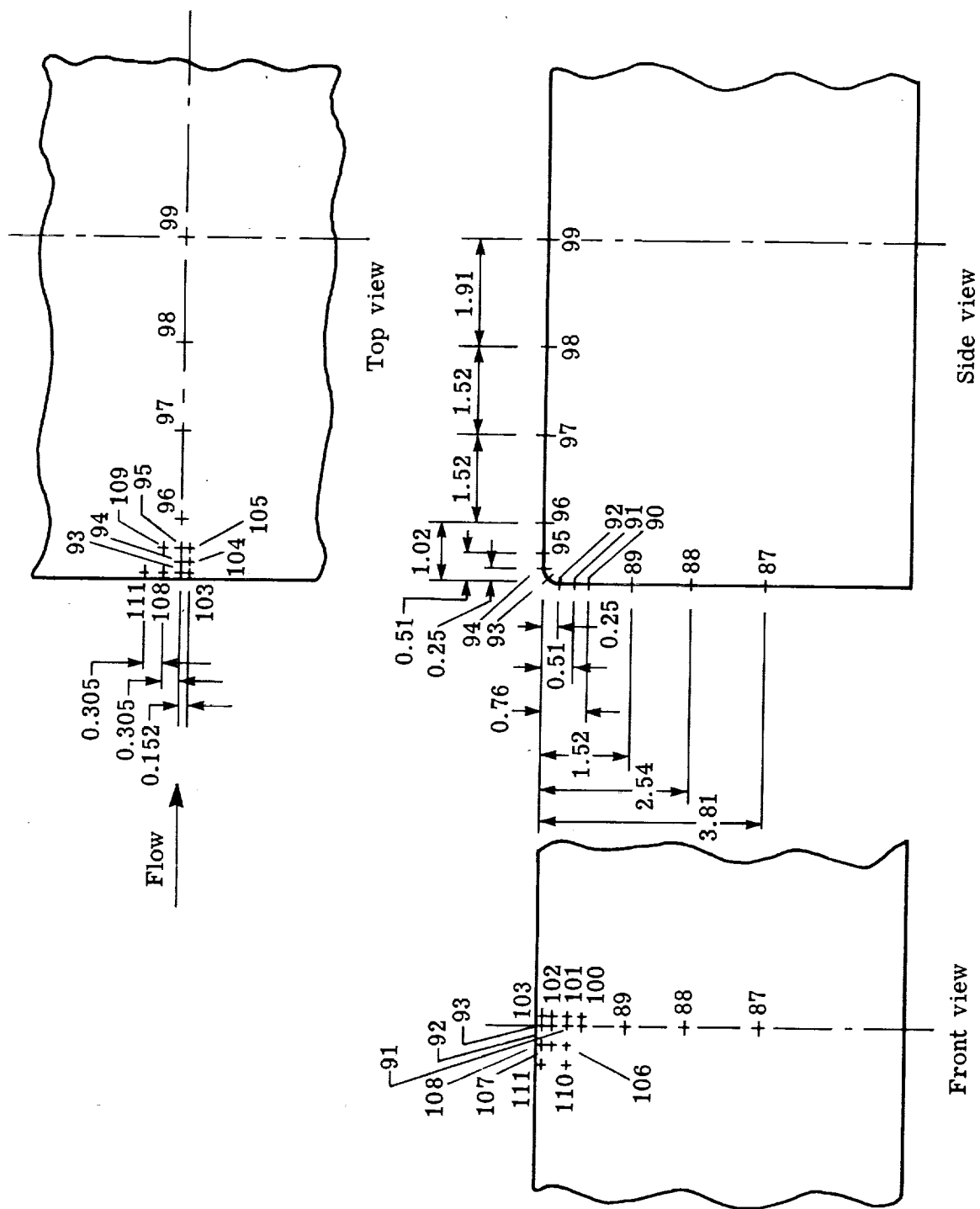


Figure 5.- Instrumentation for 90° thin wall tiles. L = 15.24 cm; dimensions are in cm. (For thermocouple designation where L = 30.48 cm, add 25 to each thermocouple number.)

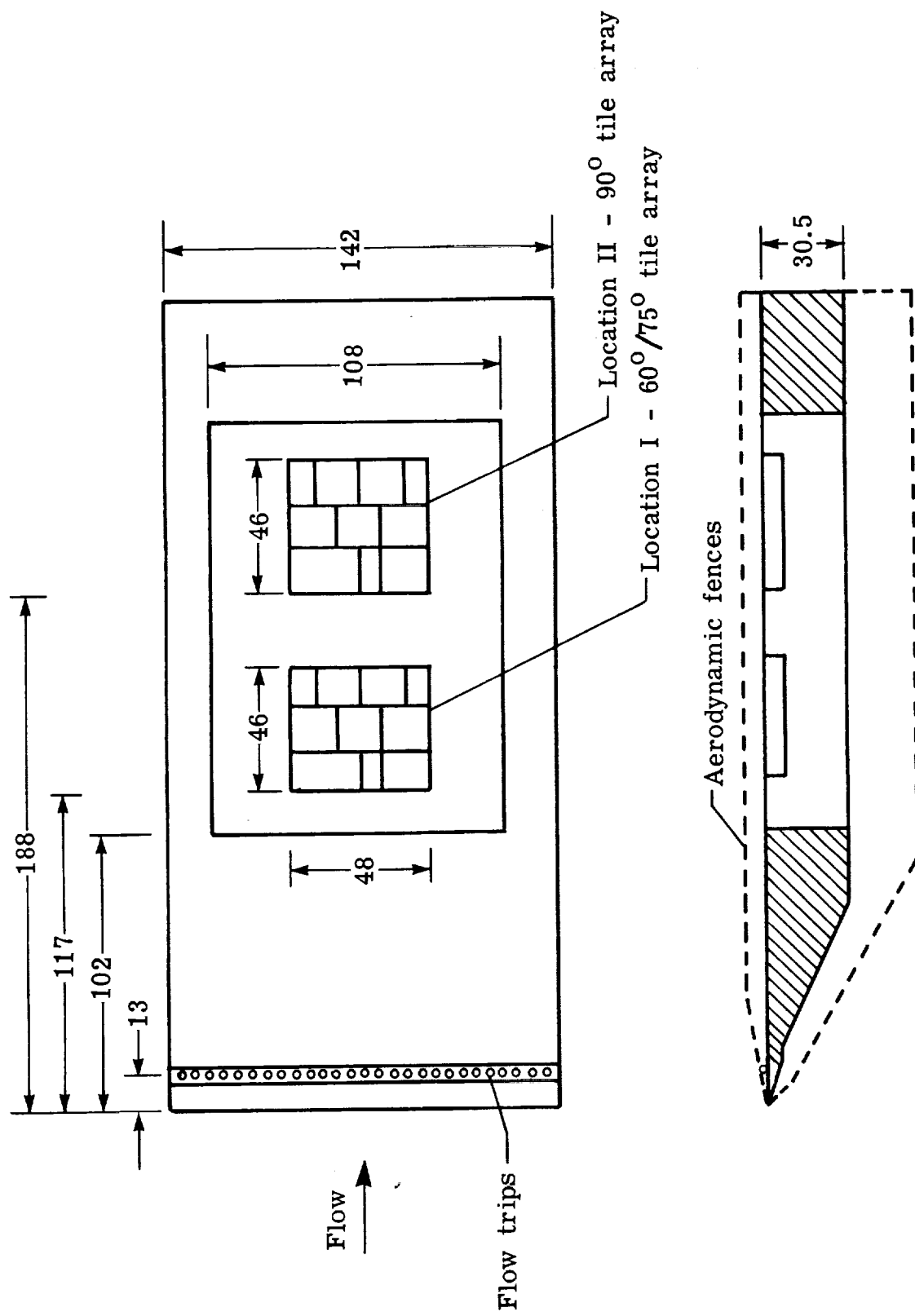
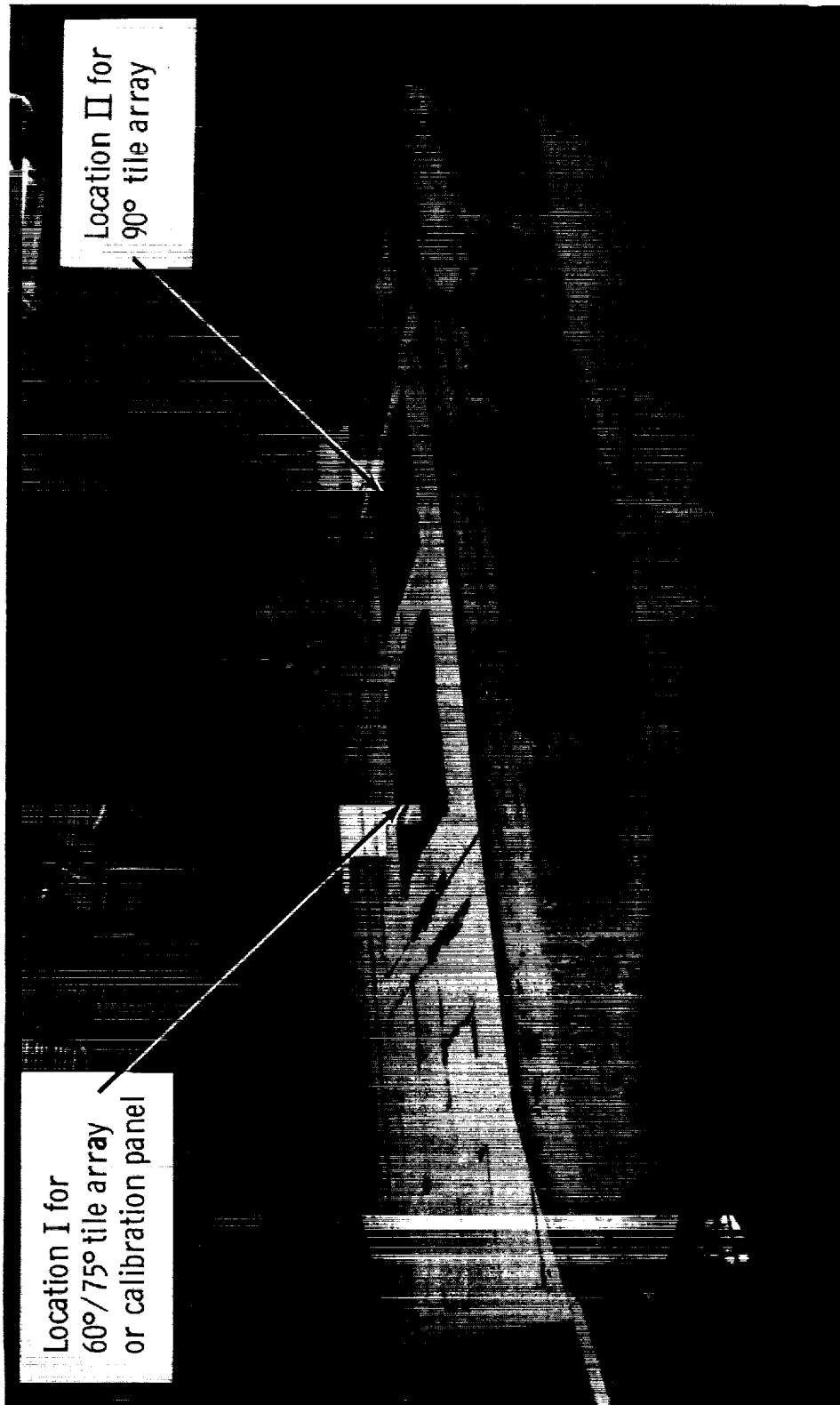


Figure 6.- Sharp leading-edge panel holder with models installed.
Dimensions are in cm.



I-75-7550.1

Figure 7.- Panel holder (with tile arrays installed) in Langley 8-foot high-temperature structures tunnel.

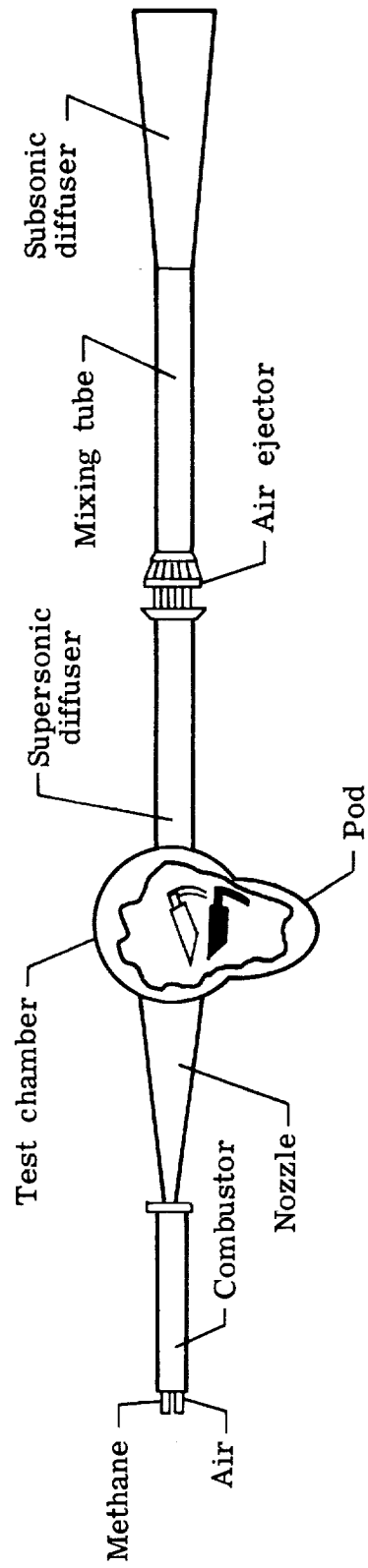


Figure 8.- Langley 8-foot high-temperature structures tunnel.

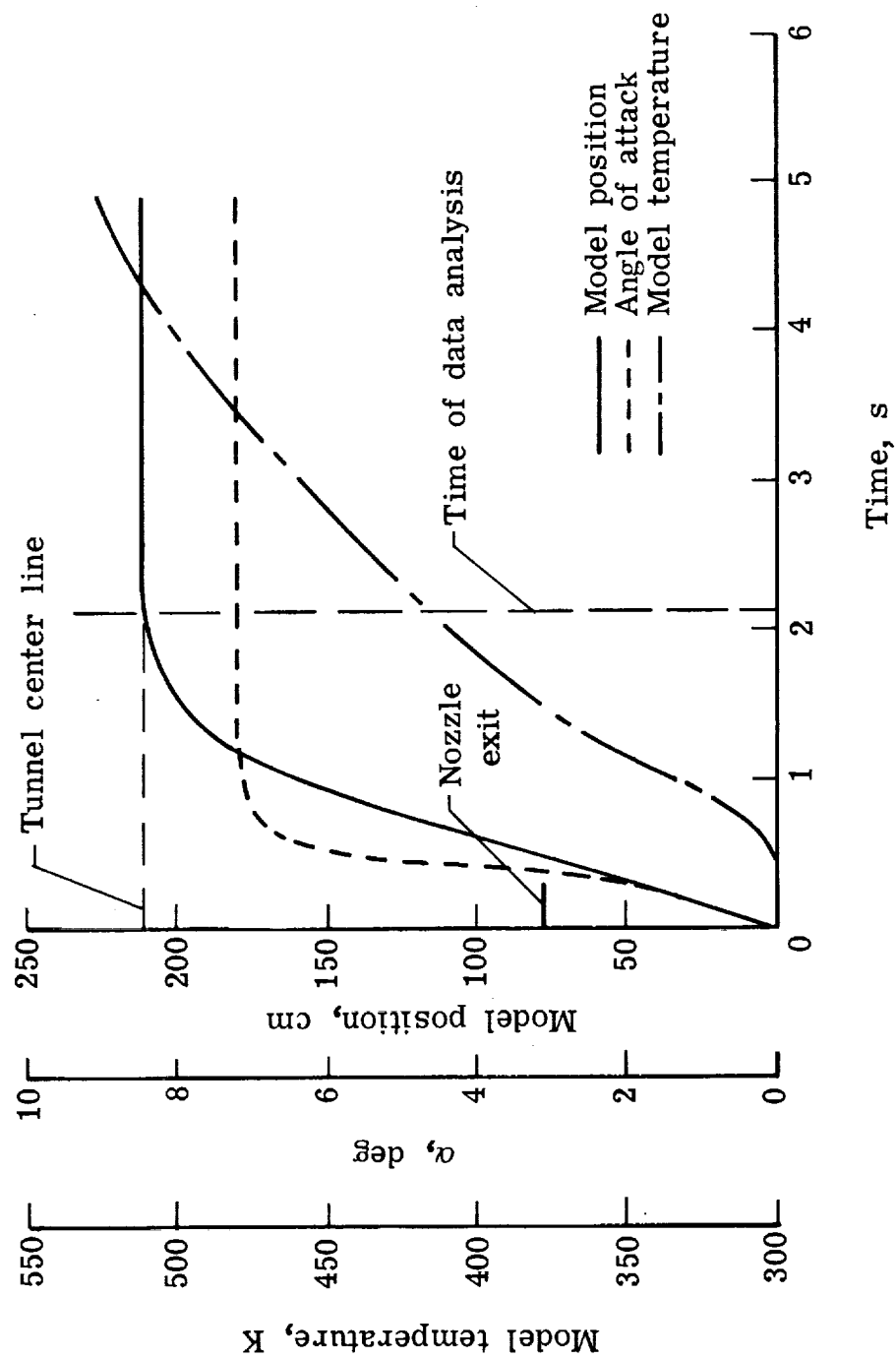
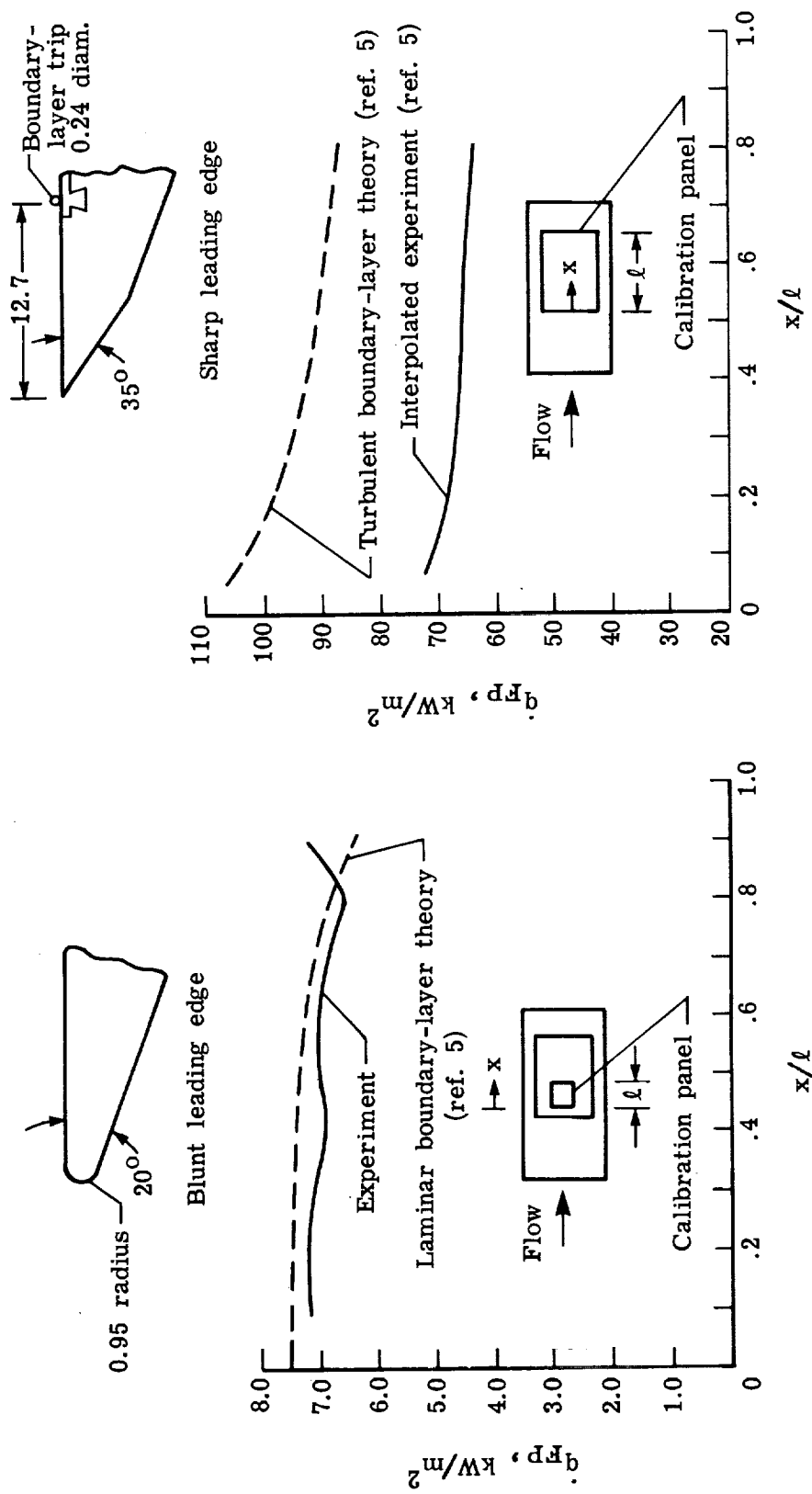


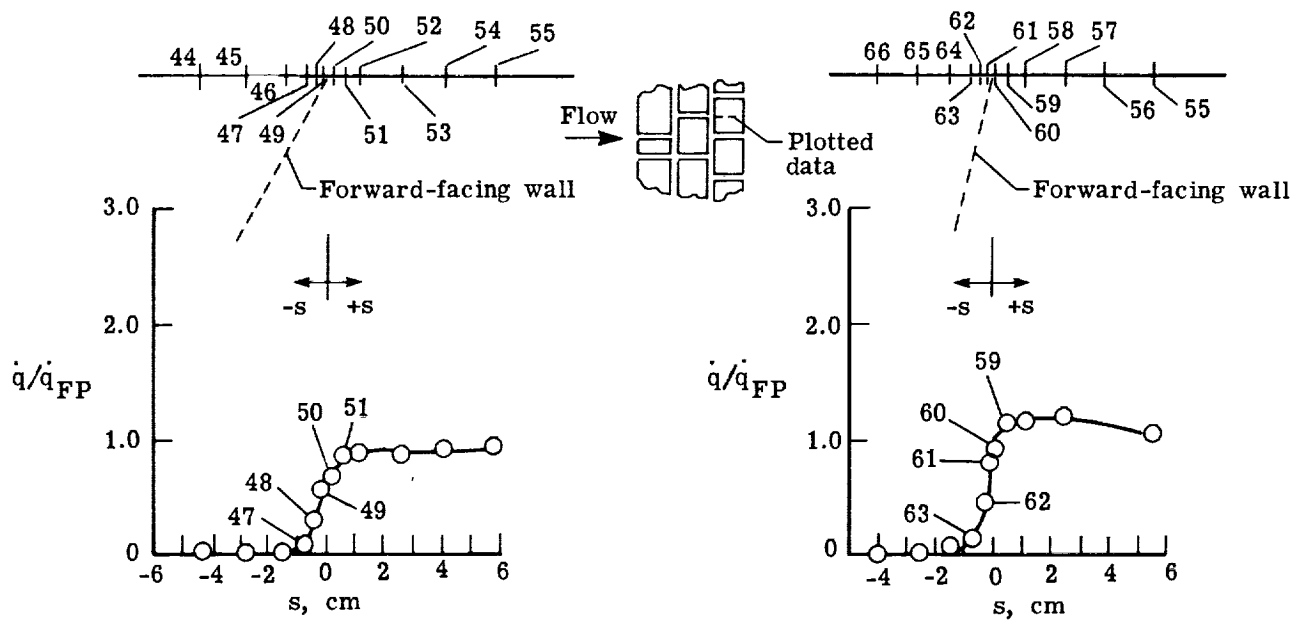
Figure 9.- Typical history of events during model injection into test stream.



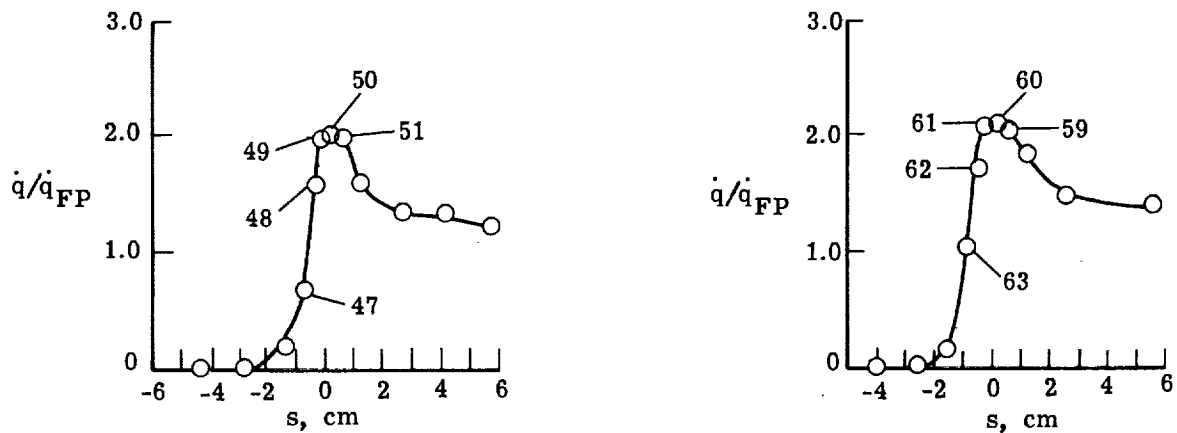
(a) Laminar boundary layer.
 $P_{t,c} = 4.3 \text{ MPa}$, $\alpha = 0^\circ$.

(b) Turbulent boundary layer.
 $P_{t,c} = 6.8 \text{ MPa}$, $\alpha = 7.5^\circ$.

Figure 10.- Typical cold-wall heating rates for calibration panels in laminar and turbulent boundary layers. Dimensions are in cm unless otherwise noted.



(a) Run 7: $\theta = 60^\circ$ and $W = 0.18$ cm. (b) Run 1: $\theta = 75^\circ$ and $W = 0.18$ cm.



(c) Run 6: $\theta = 60^\circ$ and $W = 0.41$ cm. (d) Run 5: $\theta = 75^\circ$ and $W = 0.41$ cm.

Figure 11.- Typical laminar convective heating rate distributions along longitudinal center line. $p_{t,c} = 4.3$ MPa; $\alpha = 0^\circ$; $\delta^* = 0.57$ cm; and $L = 15.24$ cm.

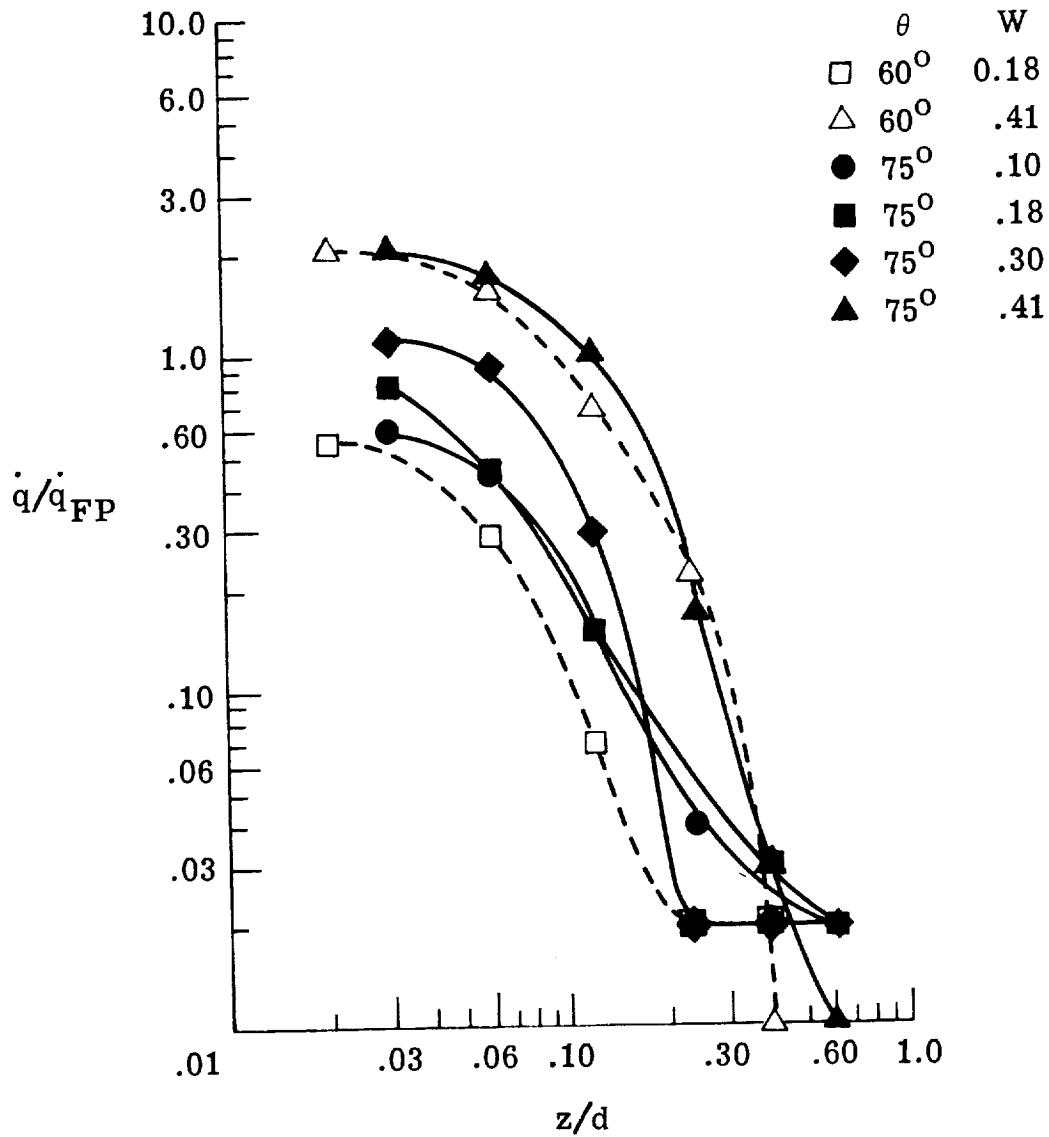
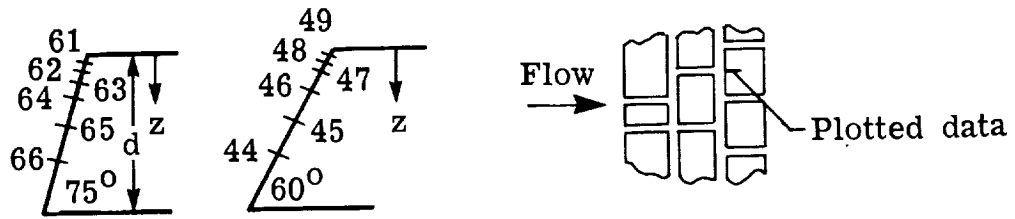
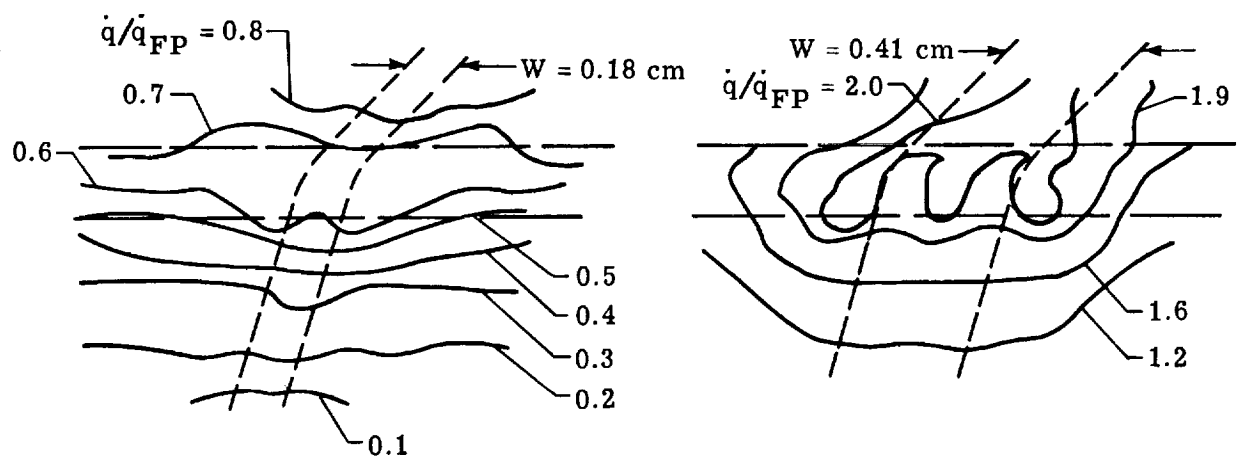
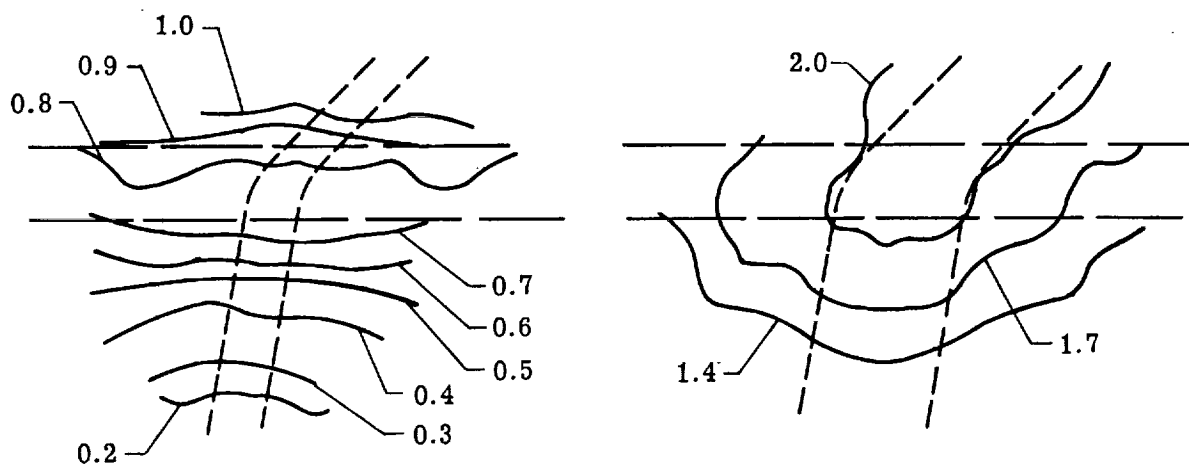


Figure 12.- Typical heating rate distributions in laminar boundary layer on forward facing walls. $p_{t,c} = 4.3$ MPa; $\alpha = 0^\circ$; $\delta^* = 0.57$ cm; $L = 15.24$ cm.

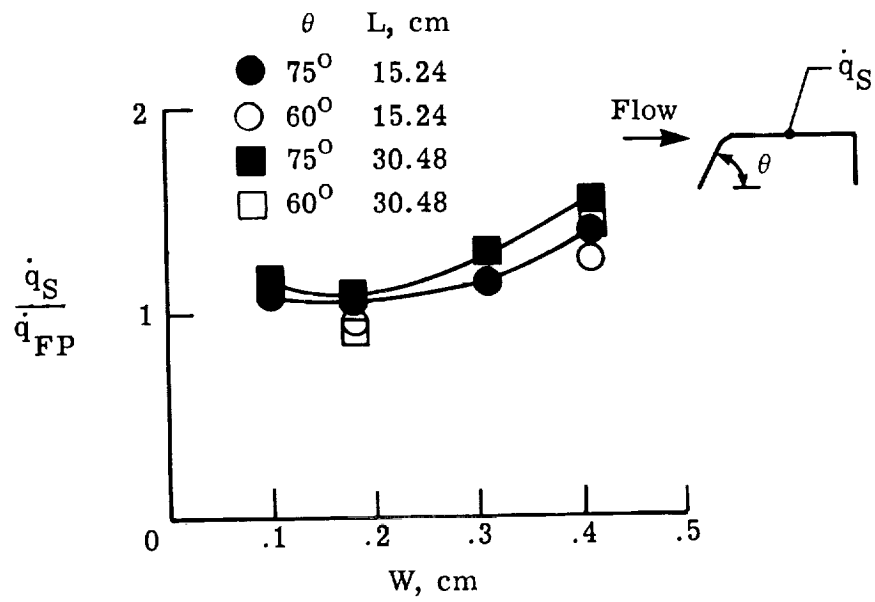


(a) $\theta = 60^\circ$.

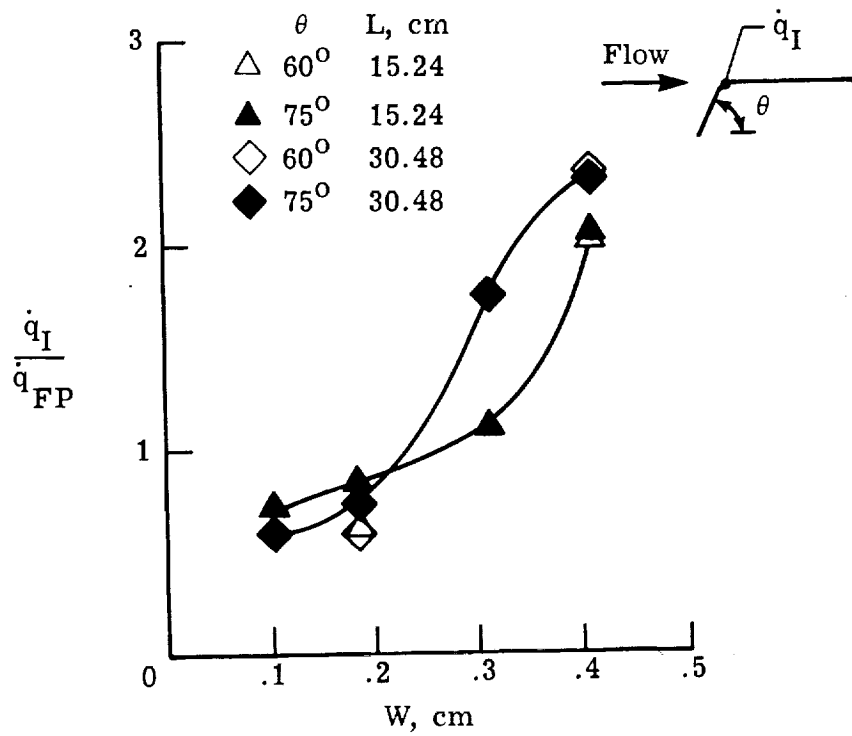


(b) $\theta = 75^\circ$.

Figure 13.- Typical isometric heating rate contour plots in laminar flow.
 $P_{t,c} = 4.3 \text{ MPa}$; $\alpha = 0^\circ$; $L = 15.24 \text{ cm}$.



(a) Surface heating.



(b) Impingement heating.

Figure 14.- Effect of gap width on surface and impingement heating in laminar flow. $p_{t,c} = 4.3$ MPa; $\alpha = 0^\circ$; $\delta^* = 0.57$ cm.

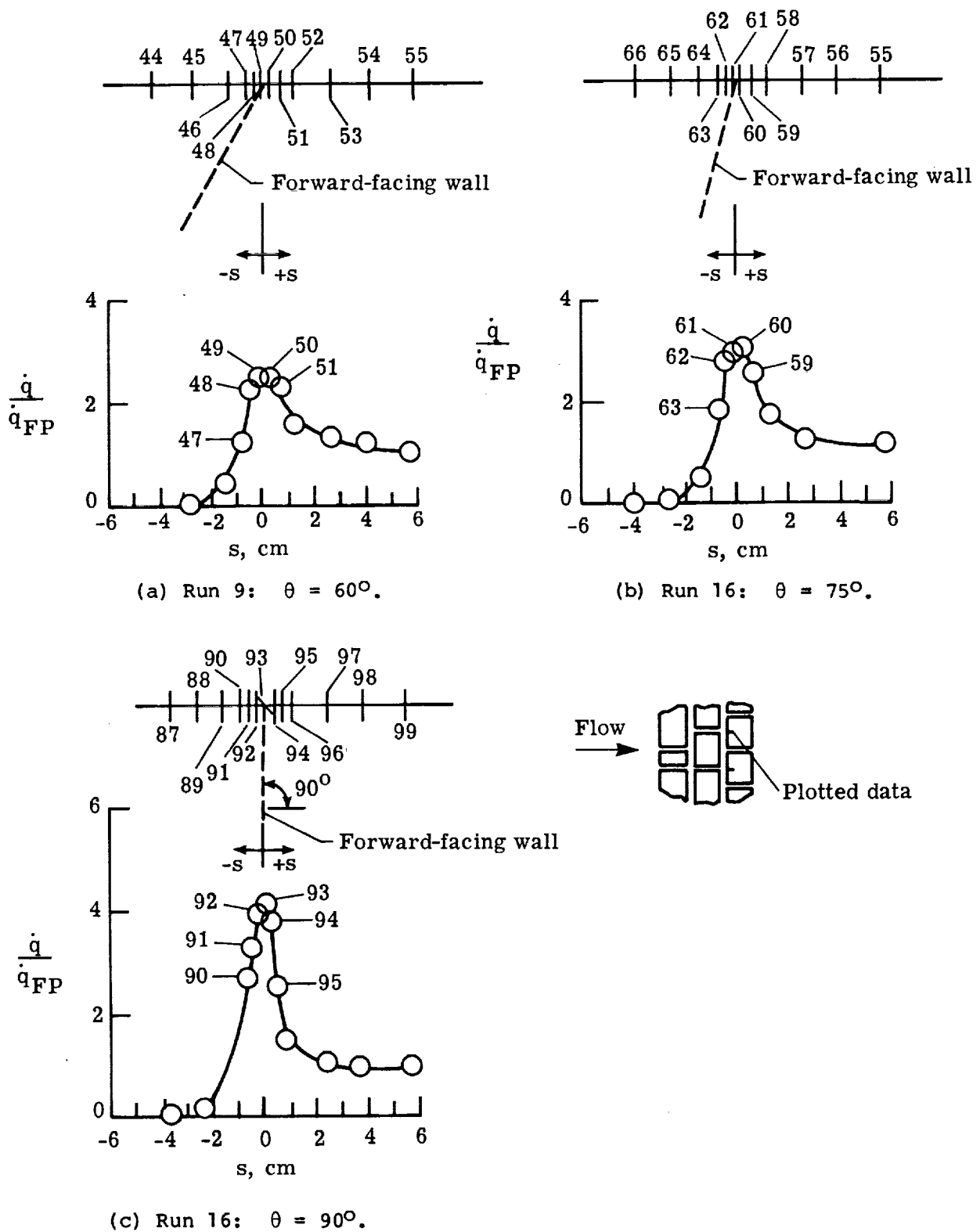


Figure 15.- Typical heating rate distributions in turbulent flow along longitudinal center line of tiles. $p_{t,c} = 6.8$ MPa; $\alpha = 7.5^\circ$; $W = 0.18$ cm; $L = 15.24$ cm.

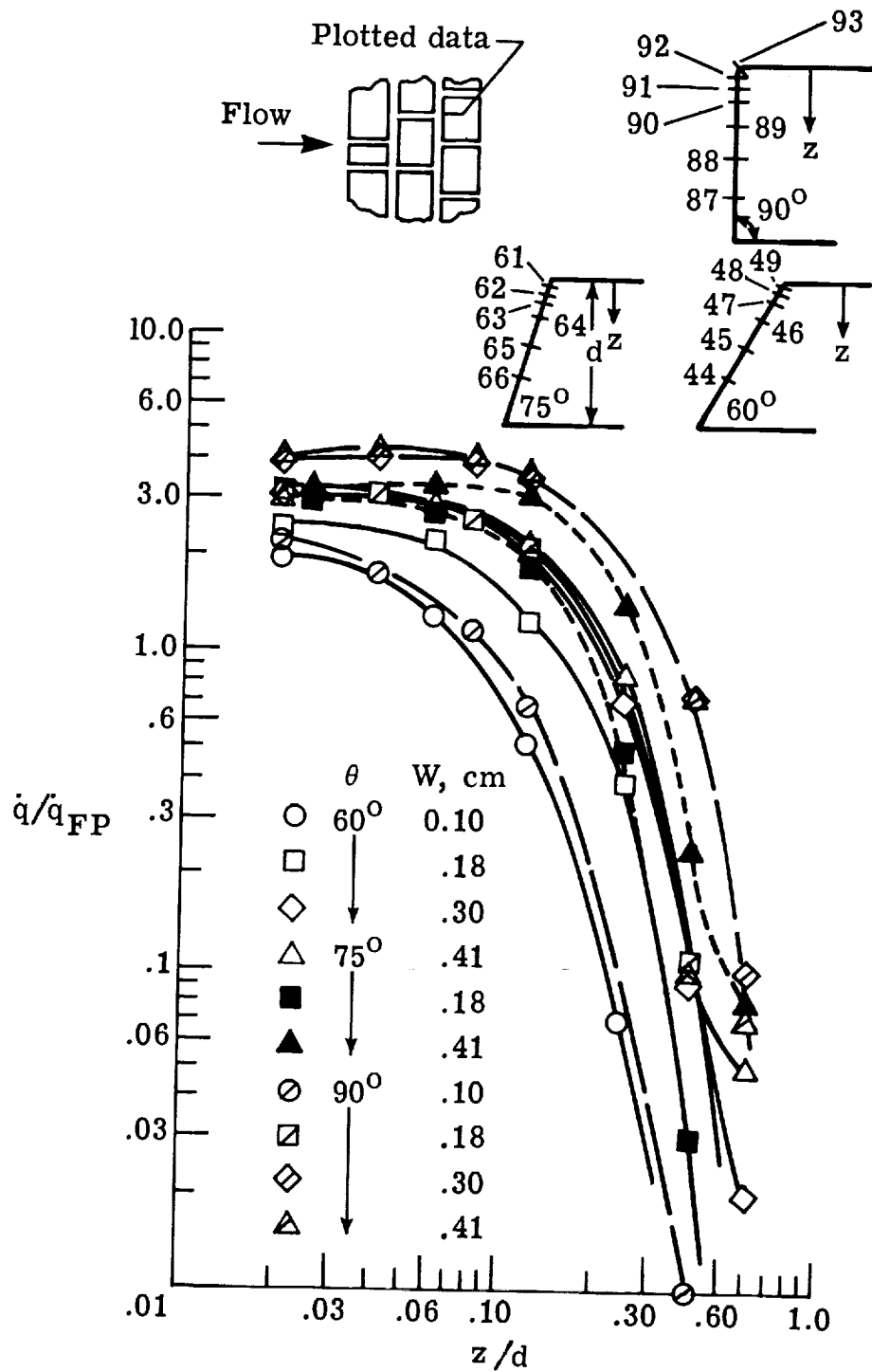


Figure 16.- Typical heating distributions in turbulent boundary layer on forward facing walls. $P_{t,c} = 6.8 \text{ MPa}$; $\alpha = 7.5^\circ$; $L = 15.24 \text{ cm}$.

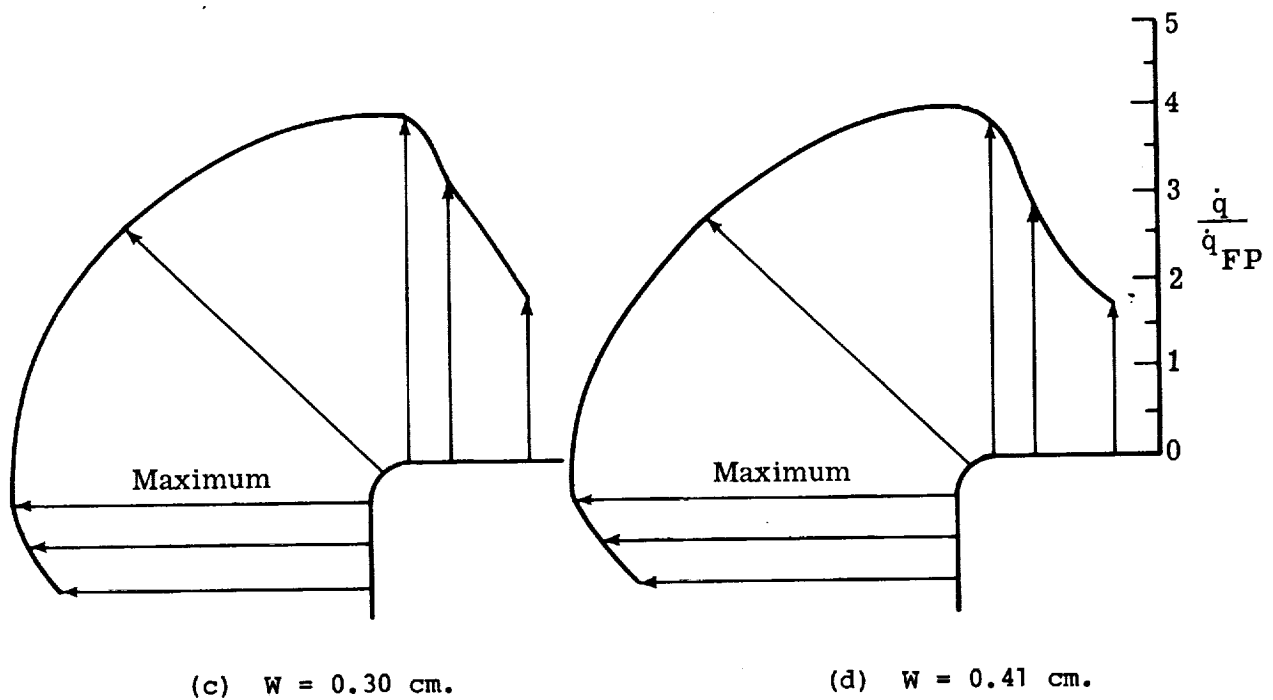
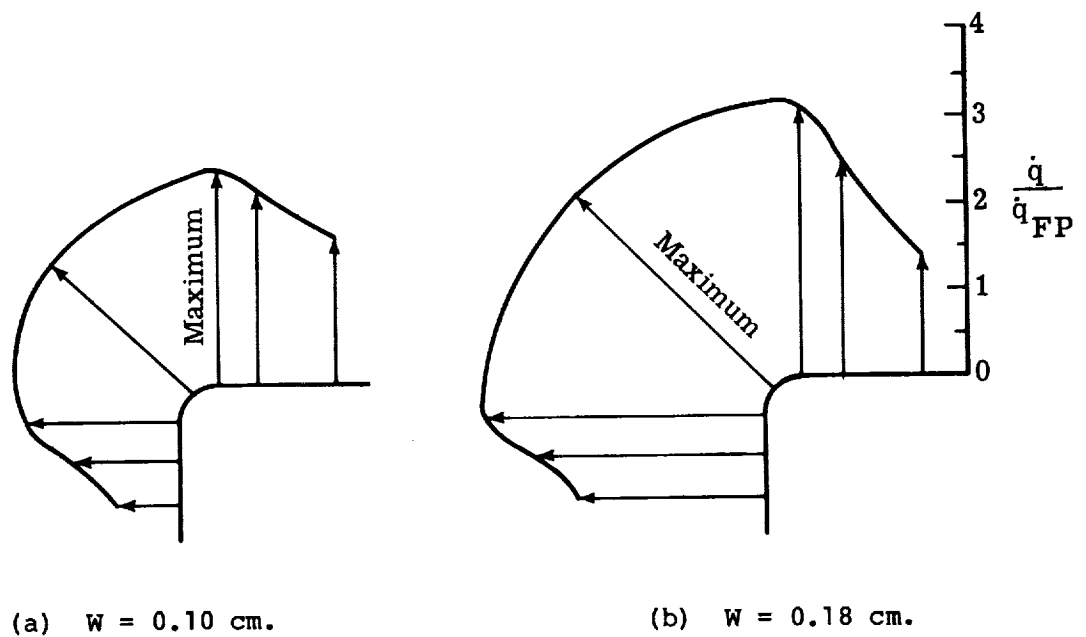
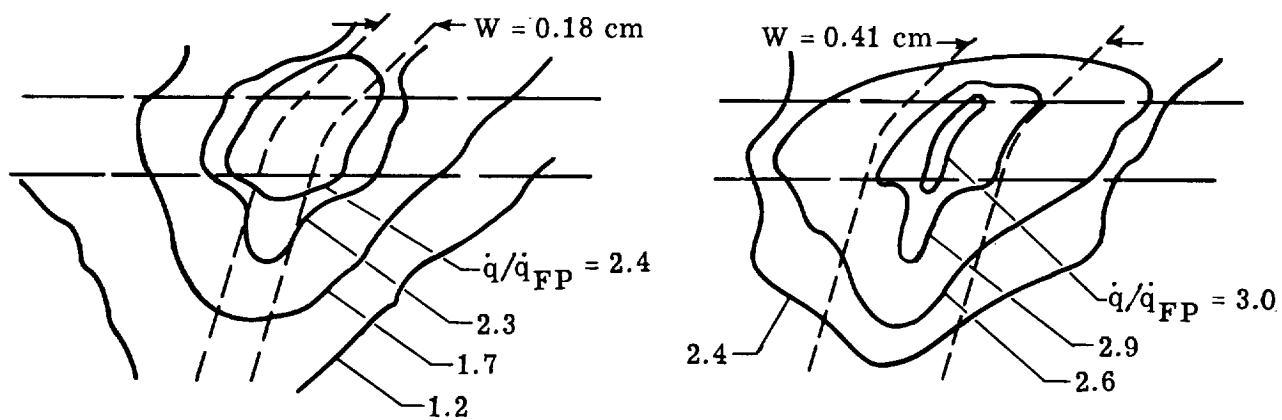
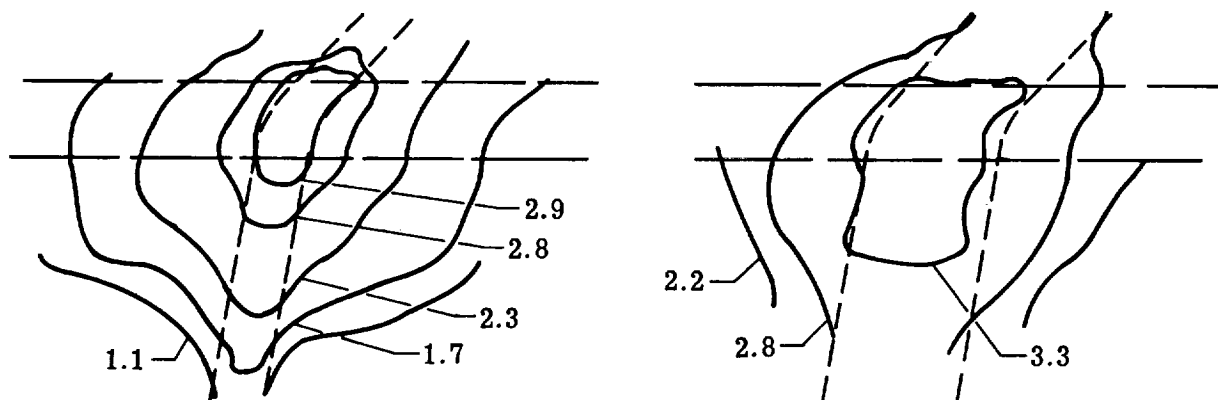


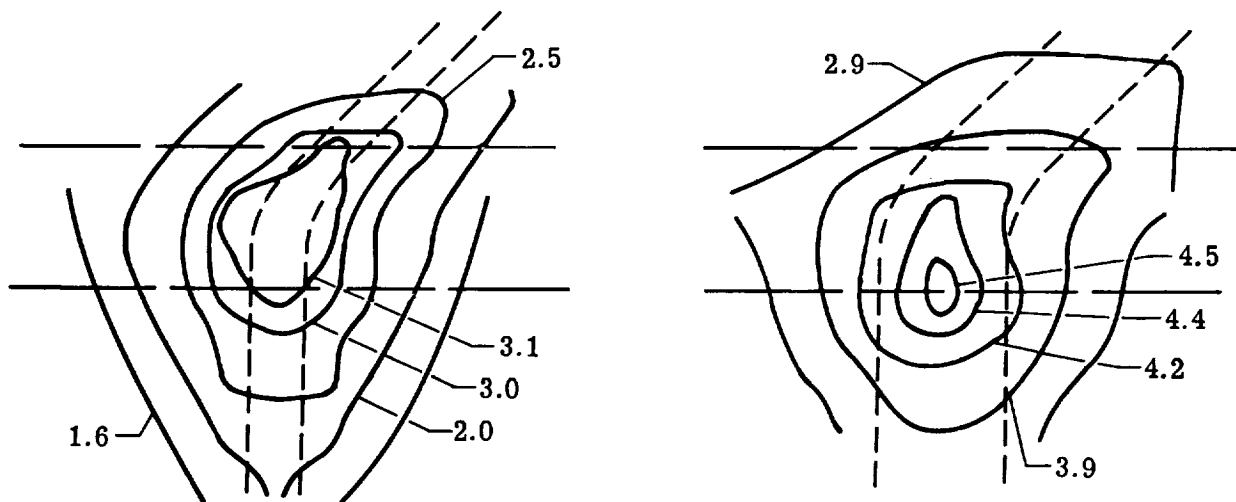
Figure 17.- Heat rate vector plots showing influence of gap width on impingement heating for turbulent boundary layer. $P_{t,c} = 6.8$ MPa; $\alpha = 7.5^\circ$; $\delta^* = 1.36$ cm; $L = 15.24$ cm; $\theta = 90^\circ$.



(a) $\theta = 60^\circ$.



(b) $\theta = 75^\circ$.



(c) $\theta = 90^\circ$.

Figure 18.- Typical isometric heating rate contour plots in turbulent flow.
 $P_{t,c} = 6.8 \text{ MPa}$; $\alpha = 7.5^\circ$; $L = 15.24 \text{ cm}$.

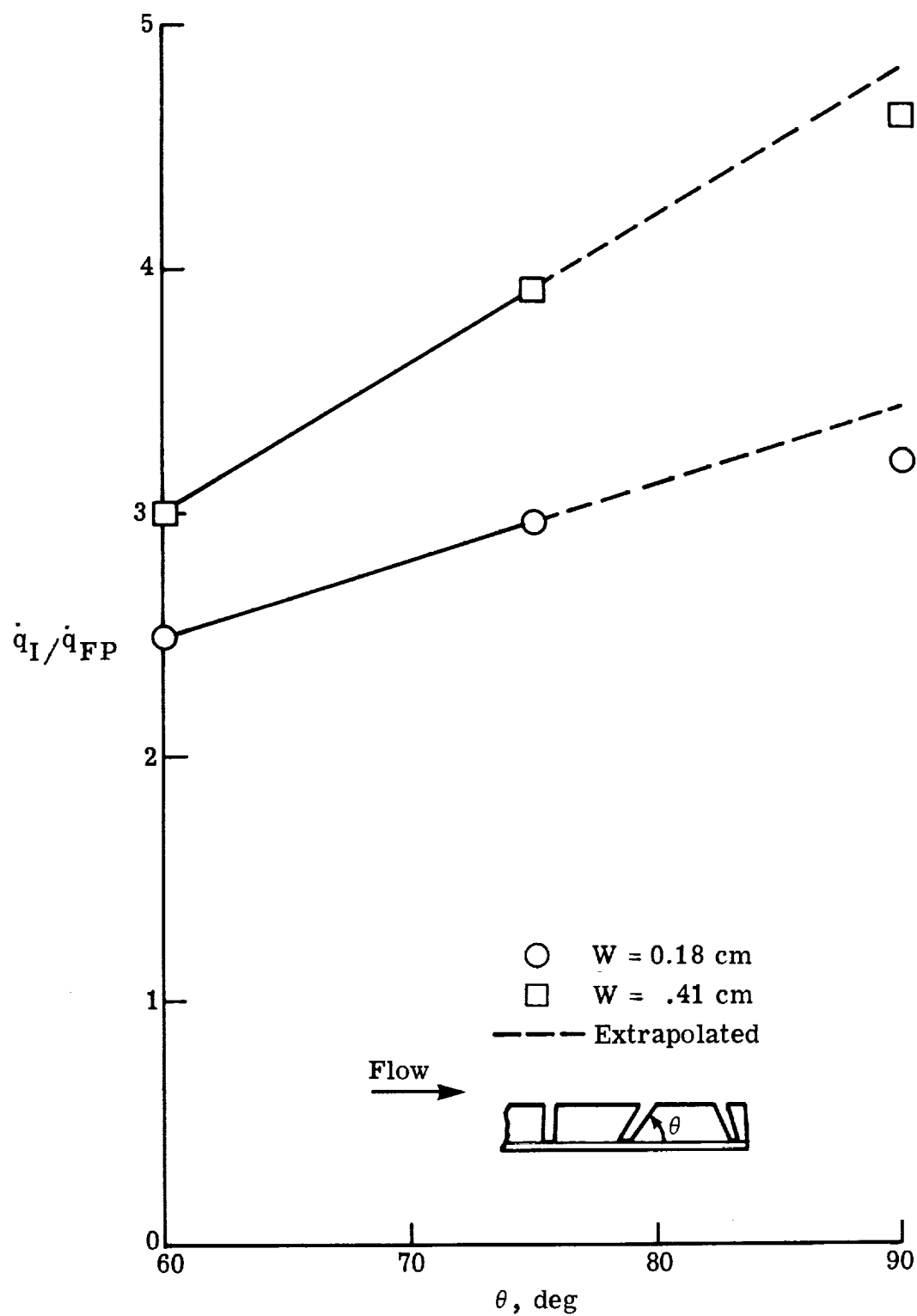
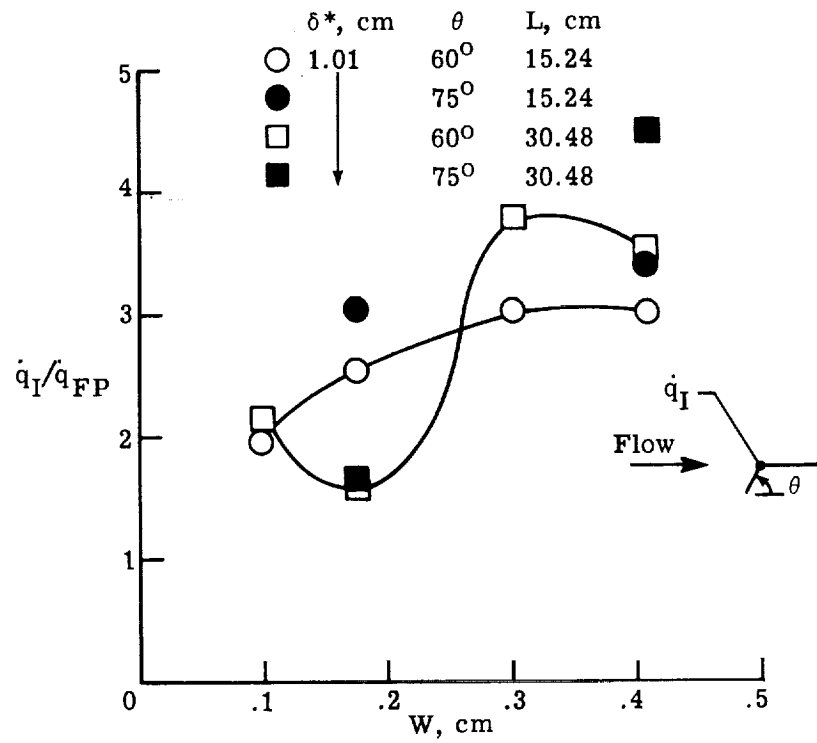
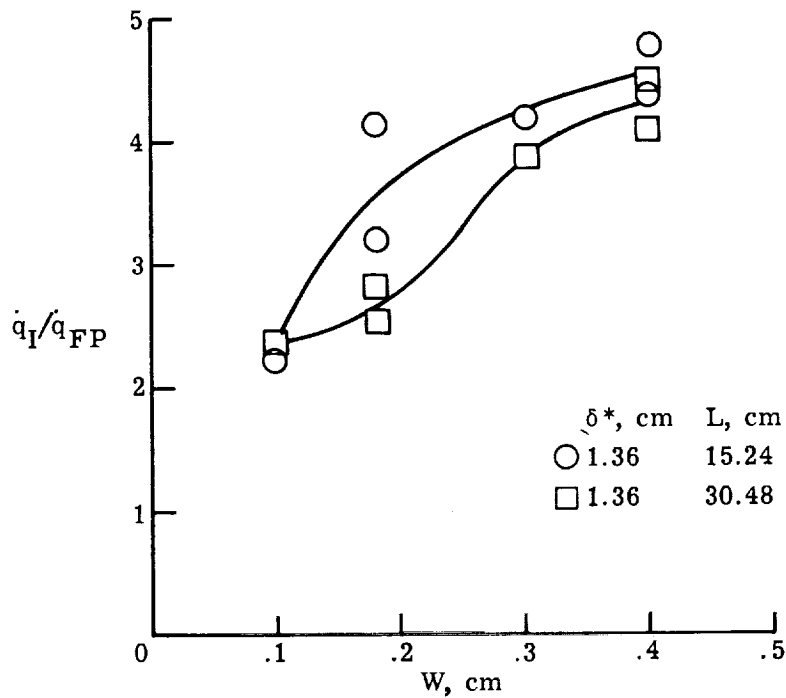


Figure 19.- Effect of slope of forward-facing wall on impingement heating in turbulent flow. $P_{t,c} = 6.8$ MPa; $\alpha = 7.5^\circ$; $\delta^* = 1.01$ or 1.36 cm; $L = 15.24$ cm.

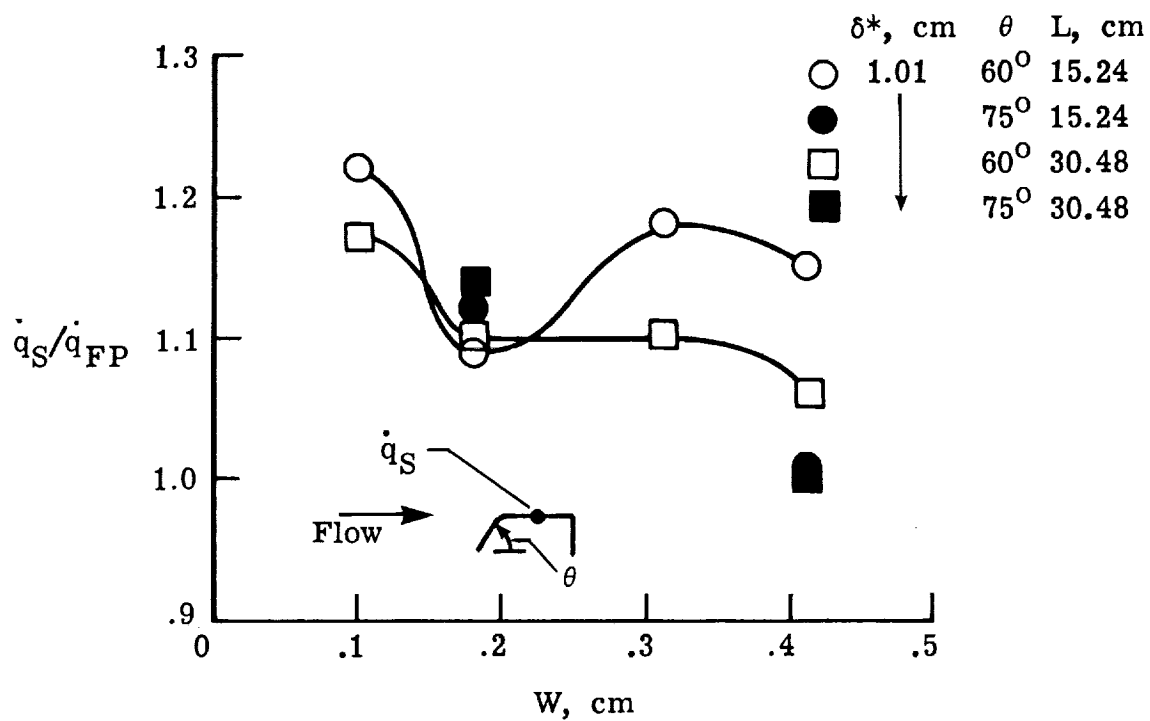


(a) $\theta = 60^\circ$ or 75° .

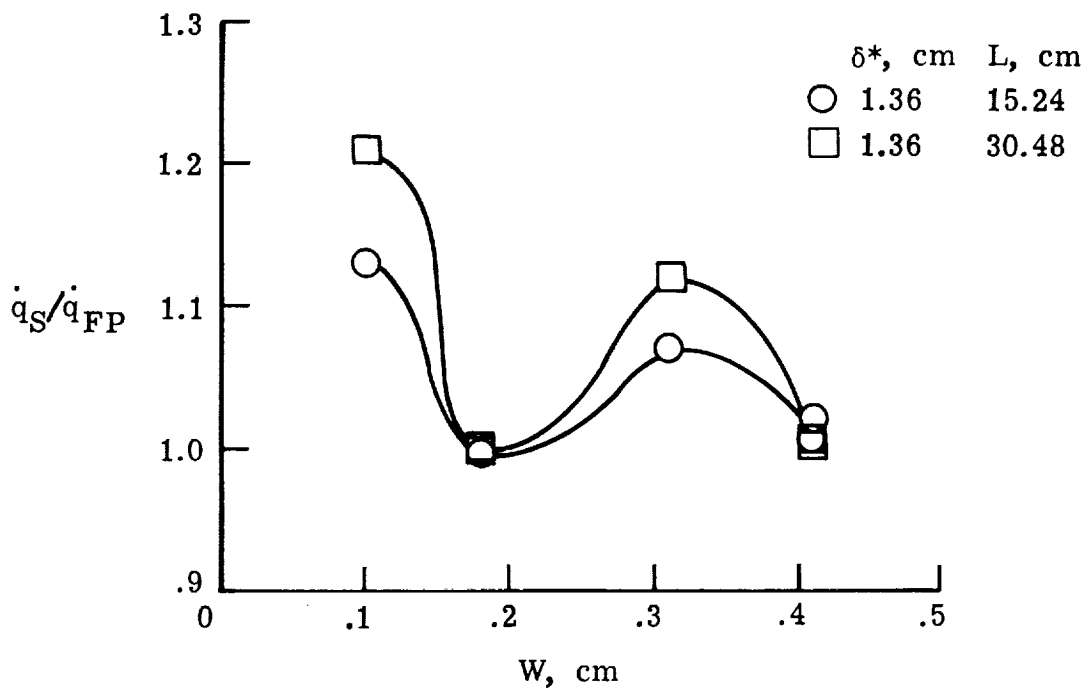


(b) $\theta = 90^\circ$.

Figure 20.- Effect of gap width and longitudinal gap length on impingement heating in turbulent flow. $P_{t,c} = 6.8$ MPa; $\alpha = 7.5^\circ$.



(a) $\theta = 60^\circ$ or 75° .



(b) $\theta = 90^\circ$.

Figure 21.- Effects of θ , W , and L on surface heating in turbulent flow.
 $P_{t,c} = 6.8$ MPa; $\alpha = 7.5^\circ$.

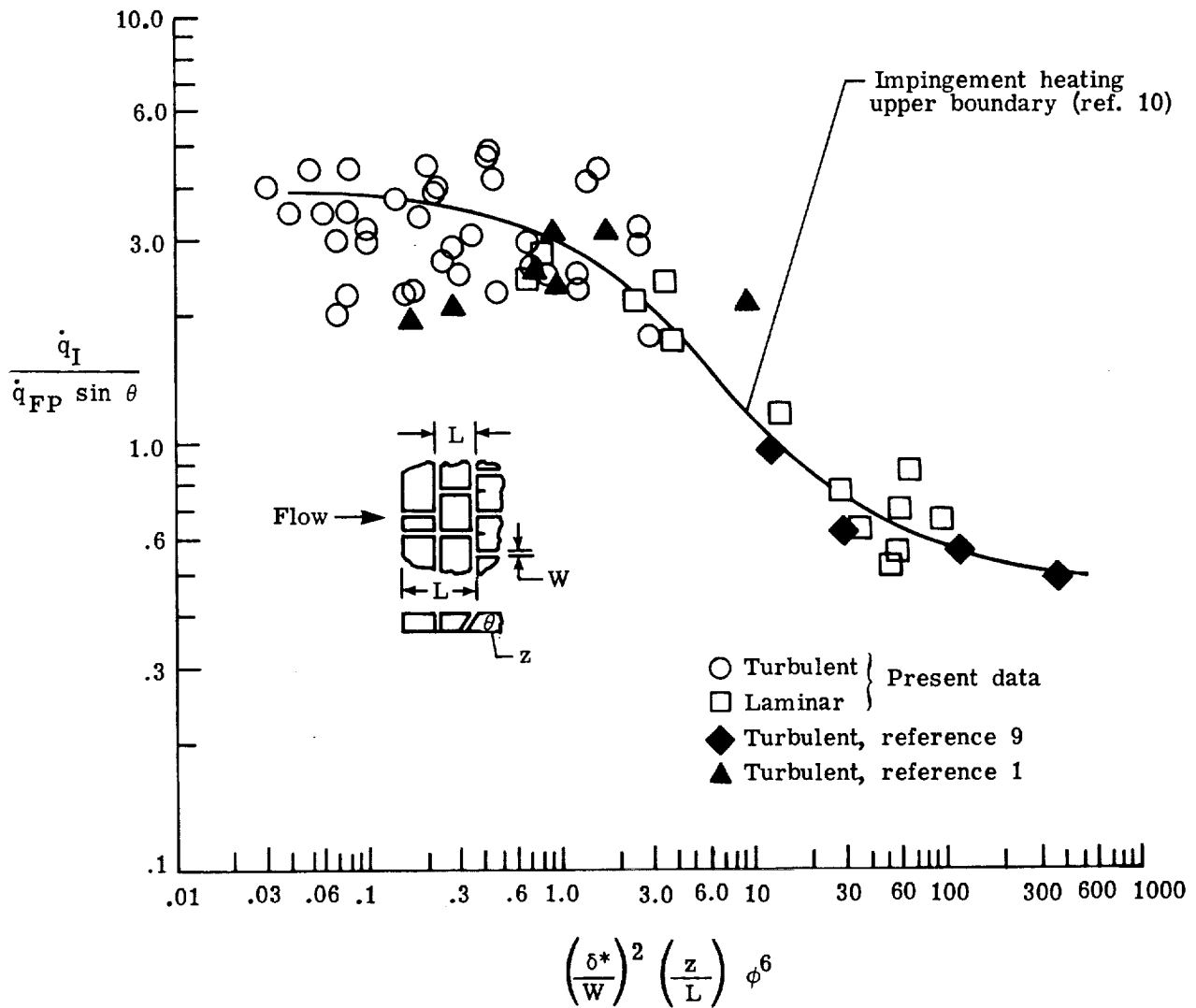
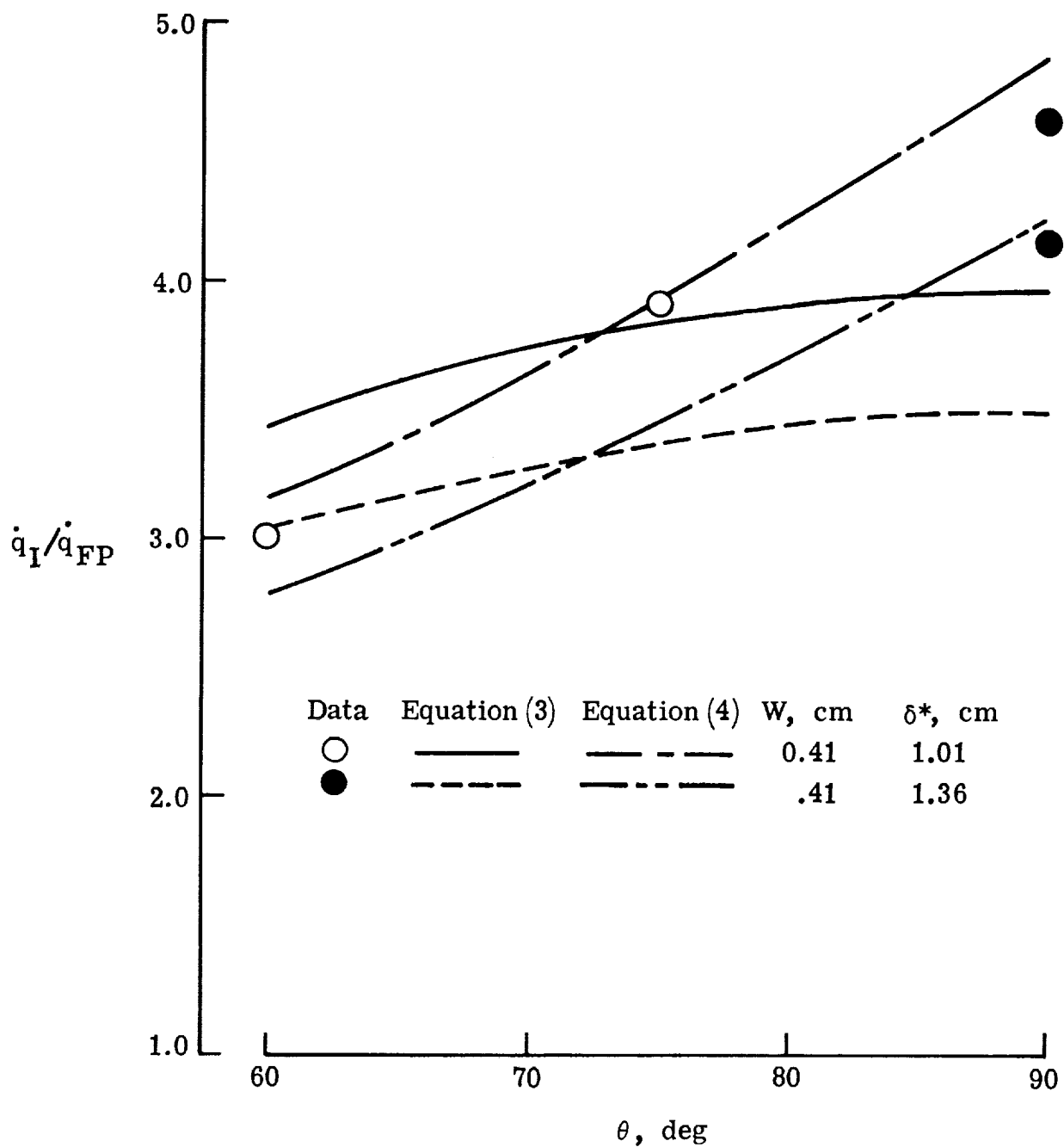
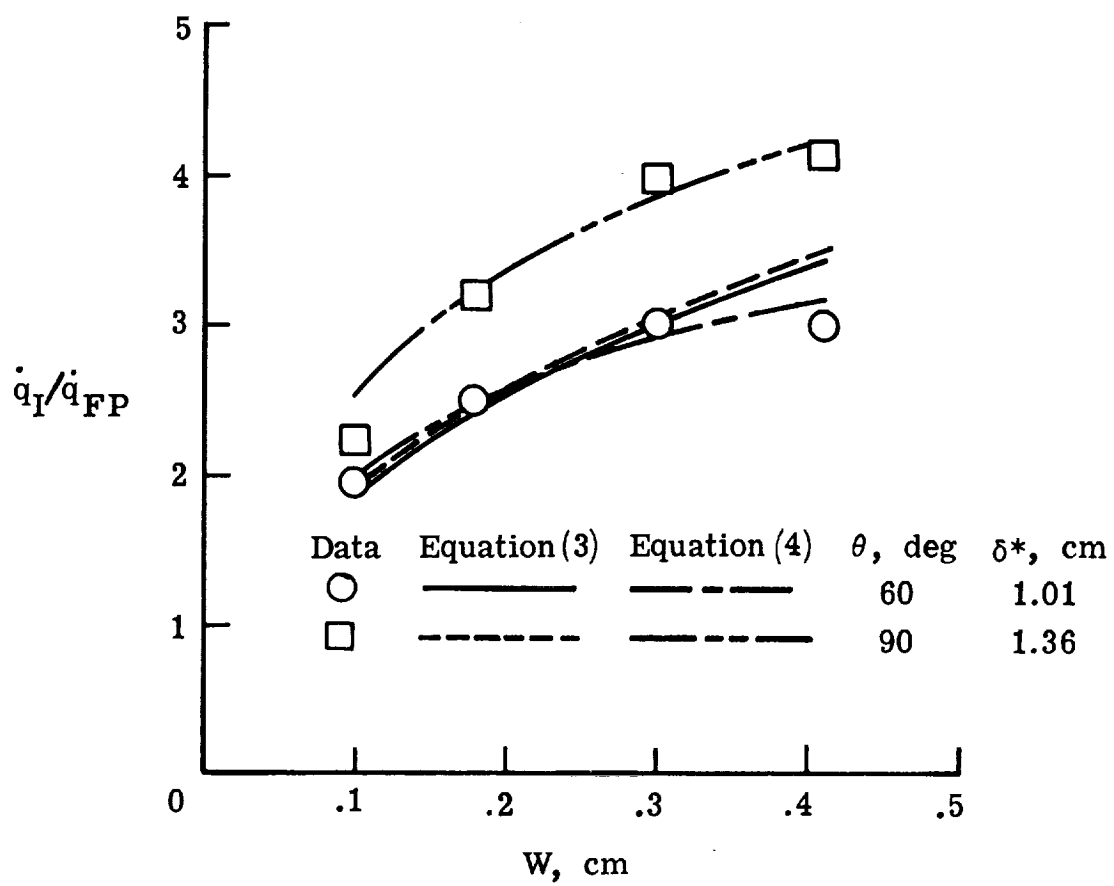


Figure 22.- Correlation of gap impingement heating data in laminar and turbulent flow.



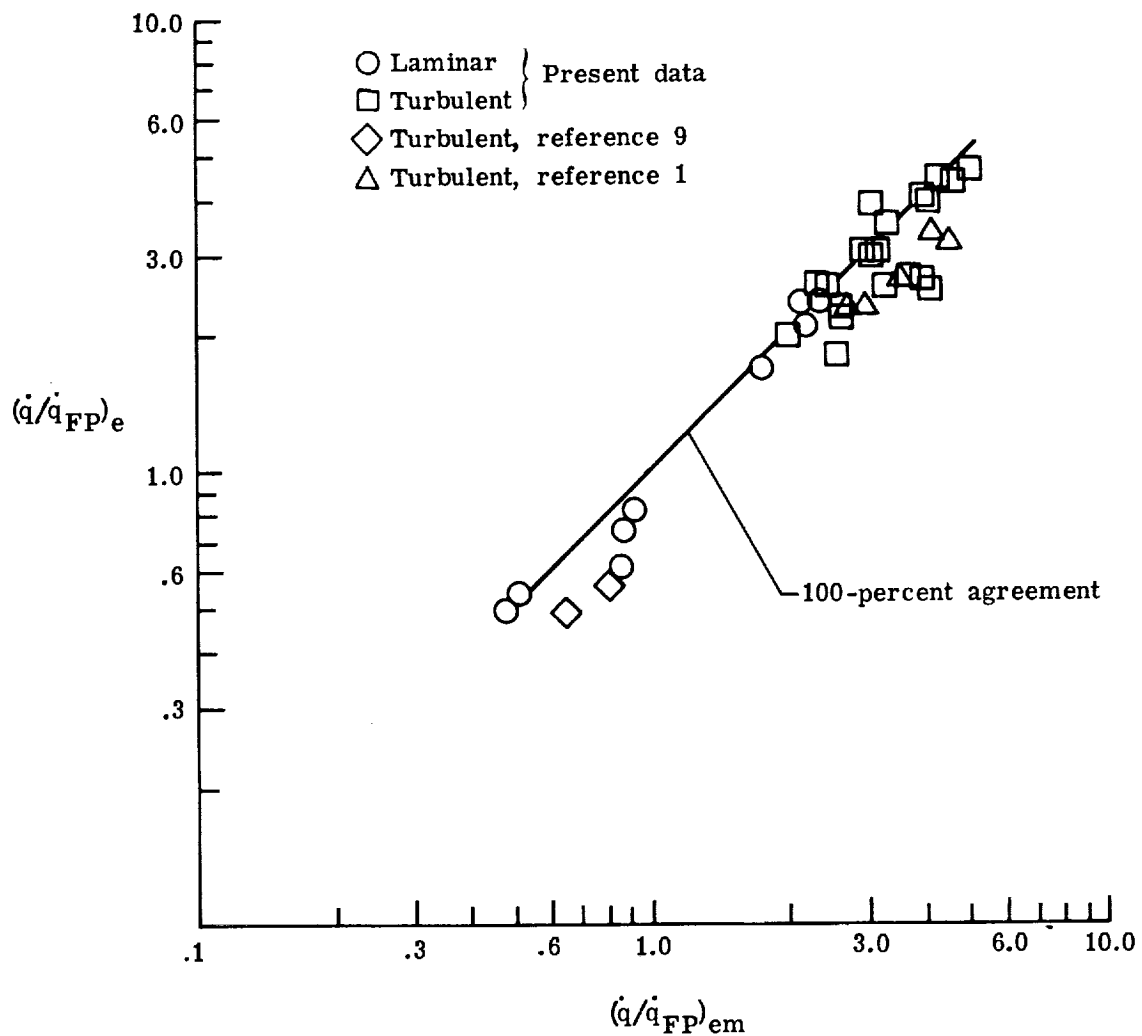
(a) Heating rate ratio plotted against θ .

Figure 23.- Comparison of empirical relationships and experimental data for turbulent flow. $L = 15.24$ cm.



(b) Heating rate ratio plotted against W . $L = 15.24$ cm.

Figure 23.- Concluded.



$$\text{Laminar: } \left(\frac{\dot{q}}{\dot{q}_{FP}} \right)_{em} = 17\,000 (\delta^*/W)^{-1.12} R_{l,L}^{-0.07} R_l^{-0.53} \sin \theta$$

$$\text{Turbulent: } \left(\frac{\dot{q}}{\dot{q}_{FP}} \right)_{em} = 5.58 (\delta^*/W)^{-0.44} R_{l,L}^{0.05} (p_S/p_{atm})^{0.18} (-0.43 W + 0.47 e^{0.70 \theta \text{ rad}})$$

Figure 24.- Empirical relationship for maximum impingement heating.



1. Report No. NASA TP-1187		2. Government Accession No.		3. Recipient's Catalog No.	
4. Title and Subtitle AERODYNAMIC HEATING IN GAPS OF THERMAL PROTECTION SYSTEM TILE ARRAYS IN LAMINAR AND TURBULENT BOUNDARY LAYERS				5. Report Date July 1978	
				6. Performing Organization Code	
7. Author(s) Don E. Avery				8. Performing Organization Report No. L-12009	
9. Performing Organization Name and Address NASA Langley Research Center Hampton, VA 23665				10. Work Unit No. 506-17-13-13	
				11. Contract or Grant No.	
12. Sponsoring Agency Name and Address National Aeronautics and Space Administration Washington, DC 20546				13. Type of Report and Period Covered Technical Paper	
				14. Sponsoring Agency Code	
15. Supplementary Notes					
16. Abstract <p>An experimental heat-transfer investigation was conducted on two staggered arrays of metallic tiles in laminar and turbulent boundary layers. This investigation was conducted for two purposes. First, the impingement heating distribution where flow in a longitudinal gap intersects a transverse gap and impinges on a downstream blocking tile was defined. Second, the influence of tile and gap geometries was defined in sufficient detail to develop empirical relationships for impingement heating in laminar and turbulent boundary layers. The tests were conducted in the Langley 8-foot high-temperature structures tunnel at a nominal Mach number of 7, a nominal total temperature of 1800 K, and free-stream unit Reynolds numbers from 1.0×10^6 to 4.8×10^6 per meter. The test results were used to assess the impingement heating effects produced by parameters that include gap width, longitudinal gap length, slope of the tile forward-facing wall, boundary-layer displacement thickness, Reynolds number, and local surface pressure.</p>					
17. Key Words (Suggested by Author(s)) Gap heating Thermal protection system Tile arrays Impingement heating Reusable surface insulation				18. Distribution Statement Unclassified - Unlimited Subject Category 34	
19. Security Classif. (of this report) Unclassified	20. Security Classif. (of this page) Unclassified	21. No. of Pages 46	22. Price* \$4.50		

* For sale by the National Technical Information Service, Springfield, Virginia 22161

NASA-Langley, 1978